Geochimica et Cosmochimica Acta 341 (2023) 62–74

Contents lists available at ScienceDirect

Geochimica et Cosmochimica Acta

journal homepage: www.elsevier.com/locate/gca

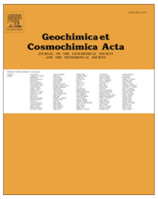

A peat core Hg stable isotope reconstruction of Holocene atmospheric Hg deposition at Amsterdam Island (37.8°S)

Chuxian Li[a,b,c,*,1], Maxime Enrico[a,b,d,1], Oliver Magand[e], Beatriz F. Araujo[b], Gaël Le Roux[a], Stefan Osterwalder[f], Aurélien Dommergue[e], Yann Bertrand[e], Jérôme Brioude[g], François De Vleeschouwer[h], Jeroen E. Sonke[b]

[a] *Laboratoire Ecologie Fonctionnelle et Environnement, Université de Toulouse, CNRS, INPT, UPS, Toulouse, France*
[b] *Laboratoire Géosciences Environnement Toulouse, Université de Toulouse, CNRS, IRD, UPS, Toulouse, France*
[c] *Department of Forest Ecology & Management, Swedish University of Agricultural Sciences, 90136 Umeå, Sweden*
[d] *Universite de Pau et des Pays de l'Adour, E2S UPPA, CNRS, TOTAL, LFCR, IPREM, 64000 Pau, France*
[e] *Institut des Géosciences de l'Environnement, Université Grenoble Alpes, CNRS, IRD, Grenoble INP, 38400 Grenoble, France*
[f] *Institute of Agricultural Sciences, ETH Zurich, 8092 Zurich, Switzerland*
[g] *Laboratoire de l'Atmosphère et des Cyclones, UMR8105, CNRS, Université de La Réunion, 97744 Saint-Denis, France*
[h] *Instituto Franco-Argentino para el Estudio del Clima y sus Impactos (UMI 3351 IFAECI/CNRS-CONICET-UBA-IRD), Universidad de Buenos Aires, Argentina*

ARTICLE INFO

Article history:
Received 16 November 2021
Accepted 22 November 2022
Available online 23 November 2022
Associate editor: Dominik Weiss

Keywords:
Hg stable isotopes
Southern Hemisphere
Peat
Rain
Hg deposition

ABSTRACT

Mercury (Hg) stable isotopes have been broadly used to investigate the sources, transformation and deposition of atmospheric Hg during the industrial era thanks to the multiple isotope signatures deriving from mass-dependent (represented by δ^{202}Hg) and mass-independent fractionation (represented by Δ^{xxx}Hg) in the environment. Less is known about the impact of past climate change on atmospheric Hg deposition and cycling, and whether Hg isotopes covary with past climate. Here, we investigate Hg concentration and Hg isotope signatures in a 6600-year-old ombrotrophic peat record from Amsterdam Island (AMS, 37.8°S), and in modern AMS rainfall and gaseous elemental Hg (Hg^0) samples. Results show that Holocene atmospheric Hg deposition and plant Hg uptake covary with dust deposition, and are both lower under a high humidity regime associated with enhanced Southern Westerly Winds. Modern AMS gaseous Hg^0 and rainfall Hg^{II} isotope signatures are similar to those in the Northern Hemisphere (NH). Holocene peat Δ^{199}Hg and Δ^{200}Hg are significantly correlated ($R^2 = 0.67$, $P < 0.001$, $n = 58$), consistently oscillating between the modern Hg^0 and rainfall Hg^{II} end-members. Peat Δ^{200}Hg and Δ^{199}Hg provide evidence of plant uptake of Hg^0 as the dominant pathway of Hg deposition to AMS peatland, with some exceptions during humid periods. In contrast to NH archives generally documenting a modern increase in Δ^{199}Hg, recent peat layers (post-1900CE) from AMS show the lowest Δ^{199}Hg in the peat profile (-0.42 ± 0.27 ‰, 1σ, $n = 8$). This likely reflects a significant change in the post-depositional process on deposited anthropogenic Hg in 20th century (i.e. dark abiotic reduction), enabling more negative Δ^{199}Hg to be observed in AMS peat. We further find that the oscillations of Hg isotopes are consistent with established Holocene climate variability from dust proxies. We suggest peat Hg isotope records might be a valid rainfall indicator.

1. Introduction

Mercury (Hg) is a global pollutant and its organic form, methylmercury, is a potent neurotoxin that harms humans (Roman et al., 2011), fish (Gentès et al., 2015) and wildlife (Scheuhammer et al., 2007). Hg released from anthropogenic Hg emissions is currently estimated to be 2400 Mg yr^{-1} (e.g., coal combustion and mining, Streets et al., 2017), which is seven times higher than primary natural emissions 340 Mg yr^{-1} (i.e. from volcanic eruptions and degassing of the Earth's crust, Li et al., 2020a). Hg is emitted to the atmosphere mainly in its gaseous elemental form (*GEM* or Hg^0, ~90%, Horowitz et al., 2017). Hg^0 deposition over the Earth's surface predominantly occurs by vegetation uptake of Hg^0 (dry deposition, Zhou et al., 2021a), and Hg^0 gas exchange with aqueous water bodies including oceans (Jiskra

---

[*] Corresponding author at: Laboratoire Ecologie Fonctionnelle et Environnement, Université de Toulouse, CNRS, INPT, UPS, Toulouse, France.

E-mail address: chuxian.li@slu.se (C. Li).

[1] These authors contributed equally.

https://doi.org/10.1016/j.gca.2022.11.024
0016-7037/© 2022 The Authors. Published by Elsevier Ltd.

et al., 2021). Hg^0 can also be oxidized to gaseous and Hg^{II} forms that are scavenged by cloud droplets or bind to aerosols, forming particulate-bound Hg. The different cloud, aerosol and gaseous Hg^{II} forms can be rapidly removed from the atmosphere by rainfall, gravitational and dry deposition respectively (Fitzgerald and Lamborg, 2003). Atmospheric Hg deposition to terrestrial surfaces varies with plant species and vegetation cover (Jiskra et al., 2018), wind-blown dust fertilization (Vandal et al., 1993) and climate (e.g., solar radiation, temperature, wind speed and rainfall, Lindberg et al., 2002; Jitaru et al., 2009; Jiskra et al., 2018; Jiskra et al., 2021; Vandal et al., 1993; Sprovieri et al., 2017).

Vegetation uptake of Hg^0 accounts for 60–90% of terrestrial Hg deposition and annually sequesters 30–70% of the modern global atmospheric Hg pool (Outridge et al., 2018; Zhou et al., 2021a; Obrist et al., 2021). The vegetation Hg pool in the Northern Hemisphere (NH) is approximately twice that in the Southern Hemisphere (SH), due to a twice larger land cover in the NH compared to the SH under similar annual climate conditions in both hemispheres (e.g., annual cloud cover, rainfall, temperature, Li et al., 2020a). Annual Hg wet deposition rate ($\mu g\ m^{-2}\ yr^{-1}$) is positively correlated with precipitation rate ($mm\ yr^{-1}$) in the NH, while this relation is less obvious in the SH (Sprovieri et al., 2017), in part due to sparser observational data. In addition, while great efforts have been put in making modern Hg observations and link trends to climate change factors (e.g., Jiskra et al., 2018; Zhou et al., 2021a; Obrist et al., 2017; Lepak et al., 2020; Wang et al., 2020), much less is known about the long-term, Holocene Hg dynamics and its interaction with past climate (Vandal et al., 1993; Jitaru et al., 2009; Sial et al., 2016; Gleason et al., 2017; Jiskra et al., 2022).

Recent work has suggested that the stable isotope composition of Hg has potential to quantify Hg deposition pathways in terrestrial (e.g., peat soils, Enrico et al., 2016) and aquatic environments (e.g., sea water, Jiskra et al., 2021). Jiskra et al., (2022) further reveals a strong link between lake sediment Hg stable isotopes and Holocene wet climate in the Southern tropical Andes, demonstrating Hg isotope signatures as a new proxy to understand paleoclimate. Hg has seven stable isotopes which can undergo mass dependent fractionation (MDF) and mass independent fractionation (MIF) in the environment (Sonke, 2011; Blum et al., 2014). MDF (represented by $\delta^{202}Hg$) is common and occurs during all physical, chemical and biotic Hg transformations (Estrade et al., 2009; Kritee et al., 2013; Zheng et al., 2019; Demers et al., 2013; Enrico et al., 2016). MIF of odd Hg isotopes (represented by $\Delta^{199}Hg$ and $\Delta^{201}Hg$) occurs mainly during aqueous photochemical Hg reduction by the magnetic isotope effect and to a much lesser extent by nuclear volume fractionation (Zheng and Hintelmann, 2010; Motta et al., 2020). Hg photoreduction has been shown to produce MIF in terrestrial foliage (Yuan et al., 2019), but no significant odd MIF is observed in biological Hg transformations (Kritee et al., 2007).

MIF of even Hg isotopes (reported as $\Delta^{200}Hg$ and $\Delta^{204}Hg$) is found to be relatively conservative at the Earth's surface. Currently, even though the mechanisms leading to even MIF still remain unclear, some studies suggest it as a result of Hg^0 photo-oxidation in the presence of aerosols above the tropopause (Chen et al., 2012), or Hg^{II} photoreduction on aerosols involving magnetic halogen nuclei and a molecular magnetic isotope effect (Fu et al., 2021). In general, background Hg^0 is characterized by slightly negative $\Delta^{200}Hg$ (−0.06 ± 0.02 ‰, 1σ, n = 71) and positive $\Delta^{204}Hg$ (0.07 ± 0.05 ‰, 1σ, n = 32, Sherman et al., 2010; Gratz et al., 2010; Demers et al., 2013; Enrico et al., 2016; Fu et al., 2016a, b; Obrist et al., 2017). Different from Hg^0, rainfall Hg^{II} is characterized by positive $\Delta^{200}Hg$ (0.16 ± 0.07 ‰, 1σ, n = 55) and negative $\Delta^{204}Hg$ (−0.16 ± 0.17 ‰, 1σ, n = 17, Gratz et al., 2010; Demers et al., 2013; Donovan et al., 2013; Enrico et al., 2016; Obrist et al., 2017; Motta et al., 2019; Washburn et al., 2021; Fu et al., 2021). The different even Hg MIF signatures in Hg^0 and rainfall allow the quantification of the two atmospheric Hg deposition pathways (Enrico et al., 2016; Jiskra et al., 2021).

Peat, formed by decomposed organic matter, sequesters Hg mainly by vegetation Hg^0 uptake and by rainfall Hg input (Enrico et al., 2016). Studies have demonstrated that Hg stable isotopes in peat cores can serve as proxies to quantify atmospheric Hg dry and wet deposition (Enrico et al., 2016), to track anthropogenic Hg pollution (Shi et al., 2011), to reconstruct past atmospheric Hg^0 concentrations (Enrico et al., 2017), to understand MIF mechanisms (e.g., magnetic isotope effect, Ghosh et al., 2008), and to identify Hg sources during springtime atmospheric mercury depletion events (Douglas and Blum, 2019). We hypothesize that variations of even-Hg MIF during the Holocene epoch reflects variable vegetation Hg^0 uptake and Hg^{II} deposition and relates to climate variables such as precipitation regimes. In this study, we use a 6600 years old peat record from Amsterdam Island (AMS) to investigate this potential use of Hg stable isotopes as a climate proxy. This site was already characterized for dust flux, which was previously found to be closely associated to climate variability (Li et al., 2020b). We combine new observations of Hg stable isotope characteristics of the modern Southern Hemisphere (SH) atmospheric Hg pool (i.e. Hg^0 and rainfall) to constrain Hg deposition mechanisms over the AMS peatland. We discuss the possible biases related to Hg cycling in peatland ecosystems, including non-photochemical and photochemical post-depositional Hg transformations. The objectives of this study are to: (i) investigate for the first time SH isotopic characterization of the different atmospheric Hg species (i.e. gaseous Hg^0 and rainfall Hg^{II}), (ii) explore the first SH mid-latitude peat Hg stable isotope variability in the Holocene and trace peat Hg cycling (i.e. deposition and potential mobility), and (iii) reconstruct Holocene rainfall based on Hg isotope signatures and compare the reconstructed rainfall profile to dust-flux-based climate dynamics.

2. Methods and materials

2.1. Study site, peat sampling and age information

AMS is a remote volcanic island located at the Southern Indian Ocean halfway between South Africa and Australia (37.8°S, 77.5°E, Fig. 1A). AMS rose up from the Ocean before 700 kyr BP. The island is ca. 9.2 km long and 7.4 km wide, which has an elliptic surface area of 55 km^2 (Frenot and Valleix, 1990) (Fig. 1B). Most of the coastline is characterized by vertical cliffs (Doucet et al., 2004). Mild oceanic conditions prevail with annual temperature of 14 °C and annual precipitation of 1100 mm (Lebouvier and Frenot, 2007). AMS is at the northern margin of the SWW, characterized by winds dominantly from west and northwest with an average speed of 7.4 $m\ s^{-1}$ (Frenot and Valleix, 1990). Air flow from continental regions is favored in austral late winter and early spring (Moody et al., 1991; Angot et al., 2014). More rainfall occurs in austral winter with on average 23 days per month of rain when the SWW seasonally shift equatorward, while in austral summer the rainfall frequency drops to 18 days per month when the SWW move poleward (Moody et al., 1991). AMS has peat deposits, with a large portion located in the caldeira at a height of 771 m a.s.l.. The 5 m long peat sequence used in this study was sampled at the caldeira peatland (Fig. 1B), which is dominated by brown moss species and *Sphagnum*. Peat core collection and age reconstruction are detailed in Li et al., (2017) and Li et al., (2020b). The last 150 years are established using a ^{210}Pb-based Constant Rate of Supply model coupled with four post-bomb dates (Li et al.,

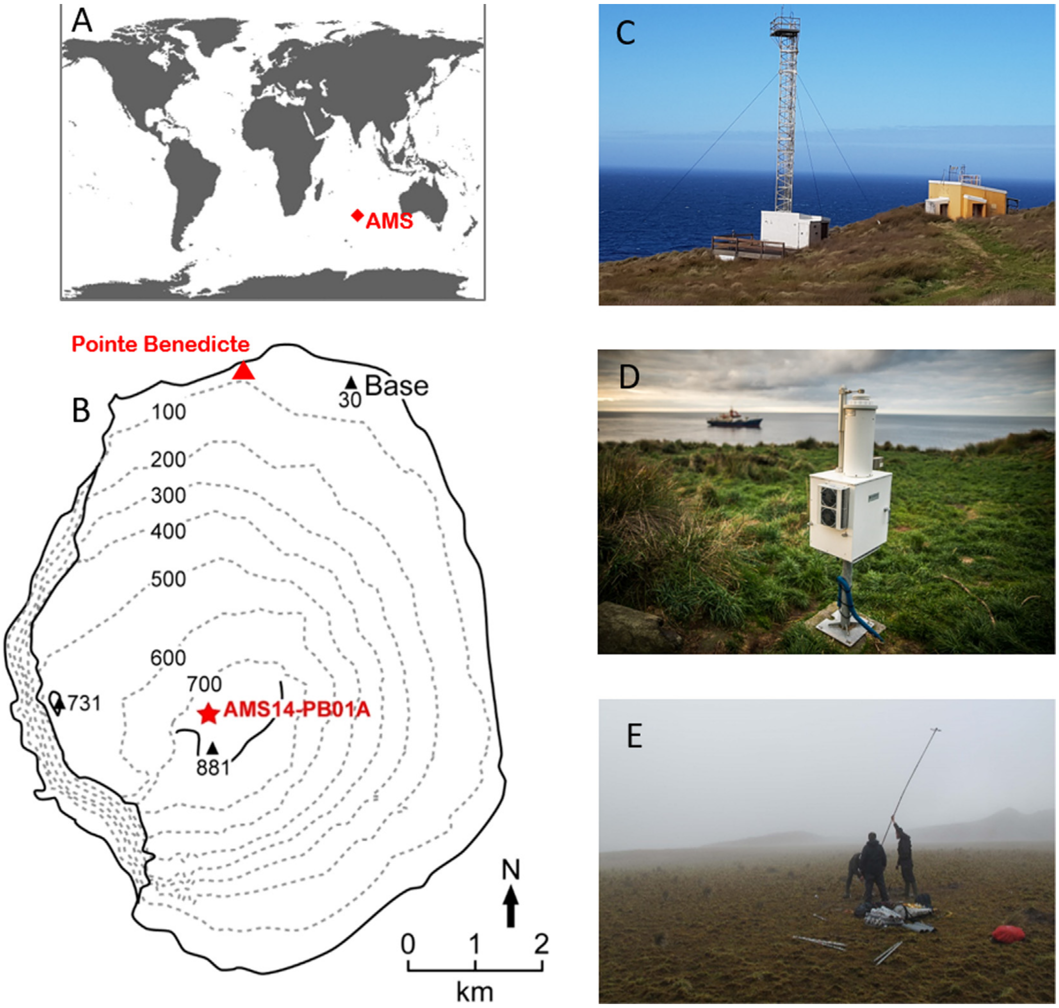

Fig. 1. (A) Location of Amsterdam Island (AMS, red diamond); (B) Sampling sites of peat core (red star, at the caldeira), rainfall and gaseous Hg^0 for isotope analysis (red triangle, at Pointe Benedicte). Black triangle at the top right represents the scientific base at AMS with 30 m above sea level. Pictures C, D and E show sampling conditions of gaseous Hg^0, rainfall and peat, respectively. Photo credit to O. Magand, I. Jouvie (C, D) and F. De Vleeschouwer (E). (For interpretation of the references to colour in this figure legend, the reader is referred to the web version of this article.)

2020b). This age model has been validated by ^{241}Am and ^{137}Cs chronomarkers (Li et al., 2017). The chronology of the deeper cores is reconstructed using ^{14}C age-depth modeling (Li et al., 2020b). This island is largely free from human disturbance. The only potential local source of pollution on this small island is from the 30-member scientific base at "*Martin-de-Viviès*" at a height of 29 m a.s.l. We expect negligible Hg pollution from the base to our peat sampling site since it is located to the southwest of the base under eastward wind flow.

2.2. Hg^0 sampling for isotope measurements

AMS atmospheric gaseous Hg^0 concentrations are thought to represent the SH background level (Angot et al., 2014; Slemr et al., 2015, 2020; Sprovieri et al., 2016). Hg^0 was collected for Hg concentration (Magand and Dommergue, 2021) and isotope analysis at the AMS Pointe Benedicte atmospheric research facility (55 m a.s.l.) located 2 km west from *Martin-de-Viviès* base (Fig. 1C). Hg^0 for isotope measurement was sampled continuously at 1.0 l min^{-1} on iodated activated carbon traps for periods of two weeks, following the published procedures (Fu et al., 2016a; Obrist et al., 2017). Twenty-five Hg^0 samples were collected from December 2017 to November 2018.

2.3. Rain sampling for Hg isotope measurements

AMS rain samples dedicated to Hg isotope measurements were collected at the AMS Pointe Benedicte atmospheric research facility (55 m a.s.l.), in an open area away from any possible contamination sources (engines / generators / fires / dust sources) from December 2017 to 2019. The collection system, consisting of four acid-washed polypropylene buckets of 20 l each, was deployed according to the forecasted rainfall events and only when major precipitation was predicted or ongoing. Buckets were deployed and fixed on top of a large polypropylene box to avoid any splash from ground that would be susceptible to contaminating the collected samples. Buckets were covered with pre-cleaned mosquito nets to collect rainfall but preventing any entry of insects or coarse particles. Buckets were put outside between 6 and 24 h depending on rainfall intensity and the filling rate of the buckets. A minimum volume of 1 l per bucket was collected to for a decent Hg isotope analysis. Once collected, rain samples were transferred to PETG 2 l bottles, and acidified with ultra-clean bi-distilled hydrochloric acid (0.036 mol/L). PETG 2 l bottles were closed as tight as possible to avoid any gaseous Hg contamination during storage and transport until analysis. Bottles were packed in double-ziploc bags in a dry, dark and clean place until transport to France. Buckets and associated materials were carefully acid-cleaned and stored between each rainfall sampling event. Note that rainfall collected using an Eigenbrodt collector for Hg wet deposition analysis is close to the base (Fig. 1D), instead of at Pointe Benedicte. We included Hg isotope signatures in rainfall samples from Maido at Reunion Island (MAI, 21.1°S, 55.4°E, 2160 m a.s.l.) and Tierra Del Fuego at the Ushuaia, Argentina (TDF, 54.8°S, 68.3°E, 272 m a.s.l.) for comparison. The methodology for rain sampling at MAI and TDF was identical to AMS.

2.4. Hg extraction and purification

Detailed information on peat sub-sampling and preparation have been shown in Li et al., (2020b). Briefly, cores were shipped by boat to France in +4 °C fridges. Cores were frozen before being sliced at roughly 1 cm resolution. Freeze-dried peat was analyzed for total Hg concentration (THg) on a Milestone Direct Mercury Analyzer (DMA80). Details of analytical performance on THg are summarized in Li et al., (2020a). Variable amounts of peat samples were used for extracting Hg for isotope measurement based on peat Hg concentration and optimum quantity of Hg required (10 ng) for a decent analysis. Hg from 58 peat samples was extracted using combustion and acid trapping methods (Sun et al., 2013). Briefly, we combusted peat samples in a double tube furnace at 1000 °C and trapped the released gaseous Hg^0 with a 40% (v/v) inverse *aqua regia* solution (2:1 HNO_3:HCl). The solution was then determined for Hg concentration by cold vapor atomic fluorescence spectroscopy (CV-AFS). The extraction yields were in the range 83–116%. We observed a matrix effect on seven peat samples leading to lower than 50% Hg recoveries during Hg isotope analysis (samples AMS 1; 62; 134; 181; 189; 200; 244). We therefore further purified the Hg in 40% (v/v) inverse *aqua regia* solutions after oven combustion. The purification system consisted of a 250 ml glass vessel where we added 10 ml sample solution, 40 ml 10% $SnCl_2$ and 150 ml Milli-Q water. The sample solution was purged by bubbling Hg free argon (300 ml min^{-1}) for 1 h into a 15 ml falcon tube with again 40% (v/v) inverse *aqua regia*. The purification yields were 93 ± 17% (n = 11, including one NIST 1632-d Coal and three international standard NIST 3133).

2.5. Hg stable isotope measurements and analytical uncertainty

Following extraction, the Hg stable isotope compositions of 58 peat samples, 21 rain samples and 23 Hg^0 samples were determined from 20% (v/v, diluted from 40%) inverse *aqua regia* solutions using cold-vapor multi-collector inductively coupled mass spectrometry (CV-MC-ICP-MS, Thermo-Finnigan Neptune, Midi-Pyrenees Observatory, Toulouse, France). Sample isotopic ratios were corrected for mass bias by sample-standard bracketing using NIST 3133 (Blum and Bergquist, 2007). Results are reported as δ-values in per mil (‰) by referencing to NIST 3133, representing to Hg mass dependent fractionation (1).

$$\delta^{XXX}Hg = \left\{\left[\left({}^{XXX}Hg/{}^{198}Hg\right)_{sample}/\left({}^{XXX}Hg/{}^{198}Hg\right)_{NIST3133}\right]-1\right\} * 1000 \quad (1)$$

MIF is calculated based on the deviations of δ-values from the theoretical MDF (2).

$$\Delta^{XXX}Hg = \delta^{XXX}Hg - \beta * \delta^{202}Hg \quad (2)$$

where XXX represents for 199, 200, 201 and 204. Symbol β is 0.2520, 0.5024, 0.7520 and 1.493 for ^{199}Hg, ^{200}Hg, ^{201}Hg and ^{204}Hg, respectively.

The quality control of Hg isotope measurements is assessed by analyzing ETH-Fluka, UM-Almaden and procedural standards (Coal, NIST 1632d, n = 4; Lichen, BCR482, n = 9). ETH-Fluka displayed δ^{202}Hg and Δ^{199}Hg of −1.43 ± 0.15 ‰ (2σ, n = 15) and 0.05 ± 0.13 ‰ (2σ, n = 15), respectively. UM-Almaden showed δ^{202}Hg and Δ^{199}Hg of −0.52 ± 0.13 ‰ (2σ, n = 7) and −0.03 ± 0.09 (2σ, n = 7), respectively. Hg isotopic signatures in procedural standards are reported in the Supplementary Information Table S1 for δ^{202}Hg (maximum 2σ = 0.15 ‰), Δ^{199}Hg (maximum 2σ = 0.09 ‰), Δ^{200}Hg (maximum 2σ = 0.10 ‰), Δ^{201}Hg (maximum 2σ = 0.12 ‰) and Δ^{204}Hg (maximum 2σ = 0.26 ‰). In this study, maximum 2σ of Hg isotopes from procedural standards is used as 2σ of each sample. When it comes to summarizing a dataset (e.g., δ^{202}Hg in all AMS Hg^0), mean and 1σ of the dataset are reported (e.g., δ^{202}Hg = 0.51 ± 0.16 ‰, 1σ, n = 23).

2.6. Hg isotope mass balance

Δ^{200}Hg in modern atmospheric end-members (Hg^0 and rainfall Hg^{II}) is thought to be conservative since no significant even MIF is measured during Hg transformations at the Earth's surface (e.g., Blum et al., 2014; Zheng et al., 2019). Although the even-Hg isotope mechanism and photo-induced redox reaction has not been identified, previous research suggested an origin at the tropopause (Chen et al., 2012). We also argue that Δ^{200}Hg in both Hg^0 and rainfall Hg^{II} end-members is relatively constant from mid to late Holocene, which is based on the absence of dramatic climate events during the last 6600 years (e.g., glacial periods) that could greatly alter the chemical reactions in the upper atmosphere leading to significantly abnormal Δ^{200}Hg production in the stratosphere (Chen et al., 2012; Fu et al., 2021). We therefore use Δ^{200}Hg in modern AMS Hg^0 and AMS rainfall Hg^{II} to quantify the atmospheric Hg deposition pathways to peat, following the equations of (3) and (4) below.

$$\Delta^{XXX}Hg_{peat} = \alpha * \Delta^{XXX}Hg_{Hg0} + \theta * \Delta^{XXX}Hg_{HgII} \quad (3)$$

$$\alpha + \theta = 1 \quad (4)$$

$$\Delta^{199}Hg_{peat-reconstructed} = \Delta^{200}Hg_{peat} * \gamma \quad (5)$$

Symbols α and θ represent the proportion of Hg^0 and rainfall Hg^{II} deposition, respectively. Only the Δ^{200}Hg of AMS rainfall with mean air pressure of trajectories above the marine boundary layers are considered. This is necessary because the site of rainfall sampling for Hg isotope analysis is at 55 m. a.s.l., while the peat sampling site is at 771 m a.s.l., which is above the marine boundary layer. We reconstructed the initially deposited Δ^{199}Hg to peatland, i.e. $\Delta^{199}Hg_{peat\text{-}reconstructed}$, using conservative Δ^{200}Hg in peat following equation (5). Parameter γ is the Δ^{199}Hg/Δ^{200}Hg slope in combined AMS Hg^0 and rainfall Hg^{II} data.

3. Results

3.1. Southern Hemisphere Hg^0 and rainfall Hg^{II} isotope signatures

Isotopic compositions of Hg^0 samples from AMS and rainfall Hg^{II} samples from AMS, MAI and TDF, are shown in Fig. 2. All of the AMS Hg0 samples are characterized by positive δ^{202}Hg (0.51 ± 0.16 ‰, 1σ, n = 23) and negative Δ^{199}Hg (−0.28 ± 0.05 ‰, 1σ, n = 23, Fig. 2A; Supplementary Information Table S2). Slightly negative Δ^{200}Hg was measured in AMS Hg^0 (−0.06 ± 0.02 ‰, 1σ, n = 23, Fig. 2B). In contrast, Δ^{200}Hg in SH rain samples was slightly positive with 0.08 ± 0.08 ‰ (1σ, n = 21). Compared to AMS Hg^0, SH rainfall samples show lower, near-zero δ^{202}Hg at AMS (0.20 ± 0.36 ‰, 1σ, n = 11), MAI (0.32 ± 0.53 ‰, 1σ, n = 3) and TDF (0.03 ± 0.41 ‰, 1σ, n = 7, Fig. 2A; Supplementary Information

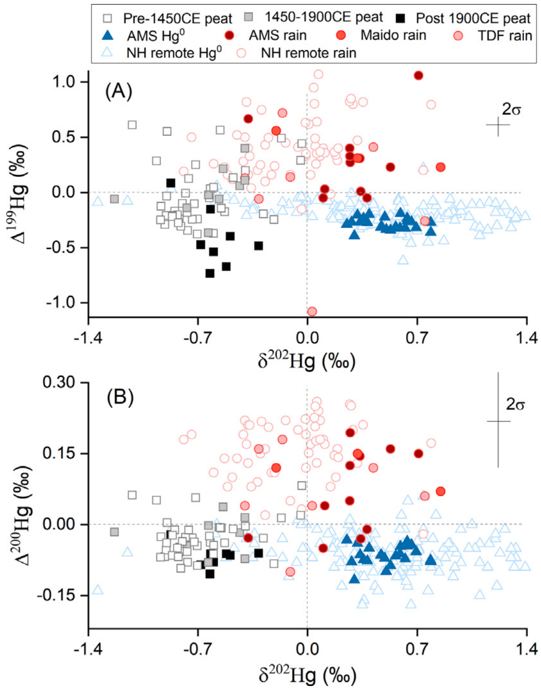

Fig. 2. (A) δ^{202}Hg vs Δ^{199}Hg and (B) δ^{202}Hg vs Δ^{200}Hg in AMS peat (squares), AMS Hg^0 (blue full triangles) and rainfall from AMS (red full dots), from Maido Observatory (MAI, La Reunion island; orange dots) and from Tierra Del Fuego (TDF, light orange dots). Peat Hg isotope signatures prior to 1450CE, between 1450CE and 1900CE, and post-1900CE, are shown in open squares, grey squares and dark squares, respectively. Red open dots represent the rainfall Hg isotope compositions from the remote areas of Northern Hemisphere (NH, refs see text), while blue open triangles represent those in the NH Hg^0 samples (refs see text). (For interpretation of the references to colour in this figure legend, the reader is referred to the web version of this article.)

Table S3). SH rainfall Δ^{199}Hg averages 0.21 ± 0.42 ‰ (1σ, n = 21), with a wide range at TDF from −1.08 ‰ to 0.72 ‰.

3.2. Peat Hg accumulation rates and isotopic signatures

AMS peat Hg accumulation rates (HgAR) and Hg isotope variability are presented according to the period divisions on AMS dust flux established using change point analysis in Li et al., (2020b). The whole HgAR profile is thus divided into six sections: 4600BCE-4200BCE, 4200BCE-3000BCE, 3000BCE-1600BCE, 1600BCE-700BCE, 700BCE-600CE, and 600CE-present. The last period is further divided into three subsections: 600CE-1450CE, 1450CE-1900CE and post-1900CE based on the onset of large-scale Spanish mining and industrial activity (Amos et al., 2015). HgAR are calculated from peat Hg concentration (ng g^{-1}), density (g cm^{-3}) and vertical accumulation rate (cm yr^{-1}), which have been detailed in Li et al., (2020a). Briefly, HgAR increase from 2.7 ± 1.7 μg m^{-2} yr^{-1} (1σ, n = 84) during the natural background period of 4600BCE-1450CE, to 8.8 ± 1.8 μg m^{-2} yr^{-1} (1σ, n = 8) during pre-industrial times of 1450CE-1880CE (Fig. 3A). HgAR profile shows maximum values during the 20th century of 14.5 ± 2.9 μg m^{-2} yr^{-1} (1σ, n = 5), followed by a decrease to 4.5 ± 1.0 μg m^{-2} yr^{-1} (1σ, n = 2) since the 21st century (Fig. 3A). The trend of post-1450CE HgAR profile echoes the historical anthropogenic Hg emission to the air in the combined sectors of South America, Africa and Oceania (Streets et al., 2019).

Peat δ^{202}Hg prior to 1450CE is characterized by negative values (Fig. 3B), ranging from −1.12 ‰ to −0.04 ‰ (average δ^{202}Hg = −0.69 ± 0.25 ‰, 1σ, n = 41, Fig. 2A; 2B; Supplementary Information Table S4). Peat δ^{202}Hg shows a general decreasing trend from 4600BCE to 1600BCE in a range of −0.21 ‰ to −1.12 ‰. Afterwards, δ^{202}Hg increases up to −0.04 ± 0.15 ‰ (2σ) at 700BCE. Peat δ^{202}Hg remains relatively constant between 700BCE and 1450CE (−0.74 ± 0.14 ‰, 1σ, n = 19, Fig. 3B). Peat Δ^{199}Hg varies from −0.38 ‰ to 0.61 ‰ and peat Δ^{200}Hg ranges from −0.09 ‰ to 0.08 ‰ prior to 1450CE. Profiles of peat Δ^{199}Hg and Δ^{200}Hg co-vary from 4600BCE to 1450CE (R^2 = 0.68, $P < 0.001$, n = 41), fluctuating at centennial time scales (Fig. 3C; 3D).

Peat δ^{202}Hg, Δ^{199}Hg and Δ^{200}Hg values during the pre-industrial period are −0.64 ± 0.25 ‰, −0.03 ± 0.23 ‰ and −0.02 ± 0.05 ‰ (mean ± 1σ, n = 10, 1450CE-1900CE, Fig. 2A; 2B), respectively, which are not significantly different from the 4600BCE-1450CE period. Again, Δ^{199}Hg is positively and significantly correlated to Δ^{200}Hg during the 1450CE-1900CE period, indicating similar atmospheric deposition origins, or similar anthropogenic Hg emission sources. Since the industrialization (post 1900CE), AMS peat δ^{202}Hg remains relatively stable with an average value of −0.59 ± 0.15 ‰ (1σ, n = 9) and is insignificantly different from the natural background period from 4600BCE to 1450CE ($P > 0.05$, two-sided *t*-test). Peat Δ^{199}Hg falls gradually from 0.40 ± 0.09 ‰ (2σ) at 1793CE to the lowest value at 1924CE (−0.73 ± 0.09 ‰, 2σ), and subsequently increases to 0.09 ‰ at 2014CE. Five Δ^{199}Hg values from 1900CE to 1975CE (−0.47 ‰ to −0.73 ‰) are more negative than modern Hg^0 Δ^{199}Hg signatures of NH remote areas (−0.18 ‰ ± 0.11 ‰, n = 157, Fig. 2A).

4. Discussion

4.1. Atmospheric Hg isotopic signatures

Both δ^{202}Hg and Δ^{199}Hg of AMS Hg^0 are similar to those in the NH remote areas (δ^{202}Hg = 0.39 ± 0.67 ‰, 1σ, n = 154; Δ^{199}Hg = −0.18 ± 0.11 ‰, 1σ, n = 157, Fig. 2A, Enrico et al., 2016; Demers et al., 2013; Fu et al., 2021; Obrist et al., 2017; Gratz et al., 2010; Sherman et al., 2010; Fu et al., 2016b; Yu et al., 2020; Kurz et al., 2020; Rolison et al., 2013; Jiskra et al., 2019). In contrast, anthropogenic emissions drive NH urban air Hg^0 to lower δ^{202}Hg (−0.33 ± 0.63 ‰, 1σ, n = 224) and near-zero Δ^{199}Hg values (−0.11 ± 0.11 ‰, 1σ, n = 224, Rolison et al., 2013; Yu et al., 2016; Xu et al., 2017; Fu et al., 2018; Yamakawa et al., 2017, 2019; Demers et al., 2015). AMS Hg^0 is identical to NH remote Hg^0 (Δ^{200}Hg = −0.06 ± 0.04 ‰, 1σ, n = 156, Fig. 2B, Enrico et al., 2016; Obrist et al., 2017; Demers et al., 2013; Fu et al., 2021; Gratz et al., 2010; Sherman et al., 2010; Fu et al., 2016b; Yu et al., 2020; Kurz et al., 2020; Rolison et al., 2013; Jiskra et al., 2019). No significant seasonal variations in AMS Hg isotopes are observed (Supplementary Information Table S2). AMS Hg^0 isotope signatures are similar to those in Antarctica (δ^{202}Hg = 0.58 ± 0.21 ‰; Δ^{199}Hg = −0.30 ± 0.10 ‰; Δ^{200}Hg = −0.08 ± 0.02 ‰, mean ± 1σ, n = 21, Yu et al., 2021), and New Zealand (δ^{202}Hg = 0.02 ± 0.27 ‰; Δ^{199}Hg = −0.30 ± 0.05 ‰; Δ^{200}Hg = −0.07 ± 0.05 ‰, mean ± 2σ, n = 4, Szponar et al., 2020). The similarities of Hg^0 isotope compositions between AMS, Antarctica, New Zealand and the NH suggest a relatively homogenous atmospheric Hg^0 isotope pool in global remote areas.

SH rainfall δ^{202}Hg is significantly higher than that in NH rainfall from remote areas (−0.08 ± 0.32 ‰, 1σ, n = 55, $P < 0.05$, two sided *t*-test, Fig. 2A, Obrist et al., 2017; Enrico et al., 2016; Demers et al., 2013; Fu et al., 2021; Gratz et al., 2010; Washburn et al., 2021; Motta et al., 2019; Donovan et al., 2013) and NH areas impacted by industrial sources (−0.66 ± 0.88 ‰, 1σ, n = 64, $P < 0.05$, two sided *t*-test, Wang et al., 2015; Zhang et al., 2020; Sherman et al., 2015, 2012). SH rainfall Δ^{200}Hg is slightly lower than that in the NH remote rainfall samples (0.16 ± 0.07 ‰, 1σ, n = 55, Obrist et al., 2017; Enrico et al., 2016; Demers et al., 2013; Fu et al., 2021; Gratz et al., 2010; Washburn et al., 2021; Motta et al.,

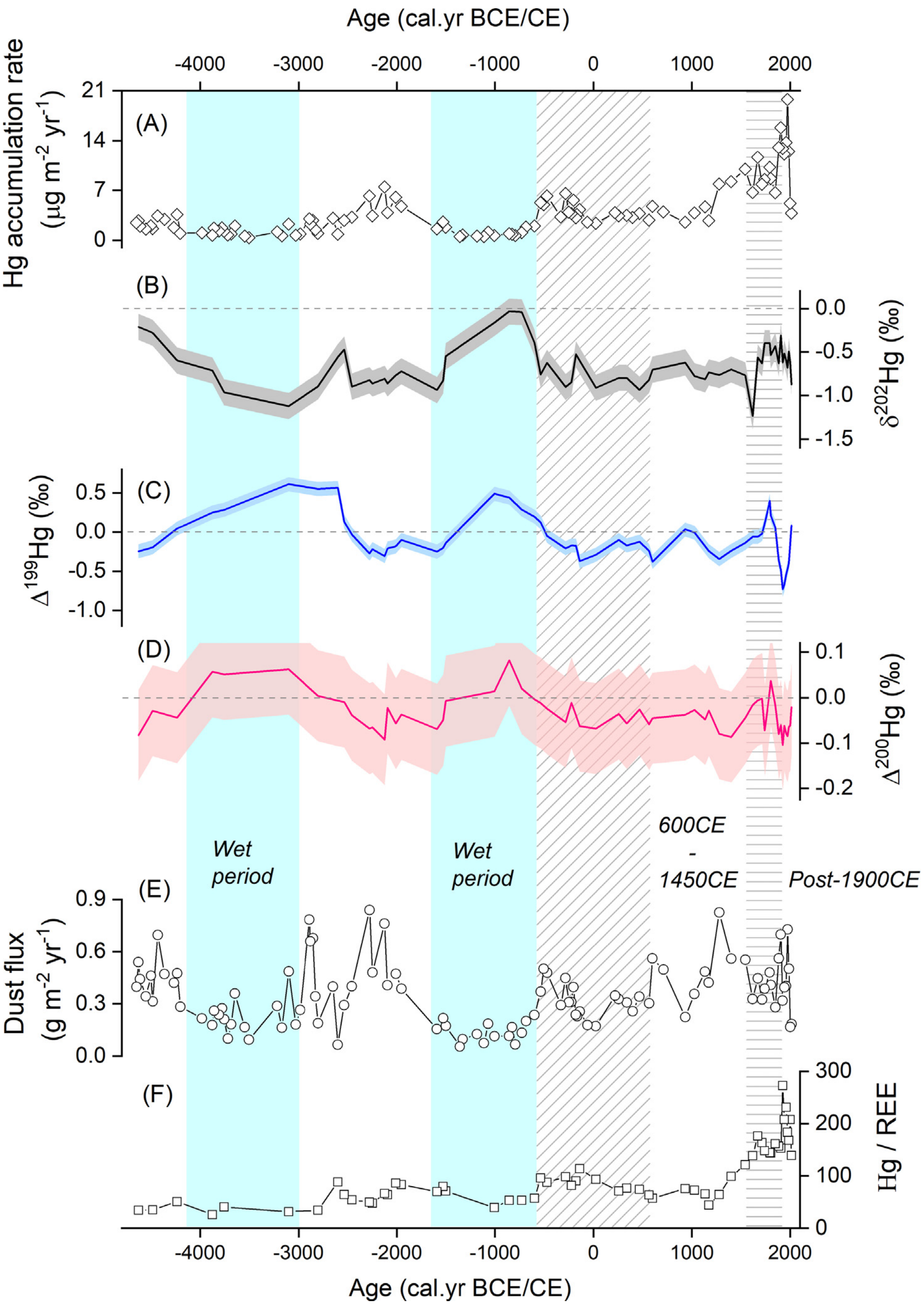

Fig. 3. Profiles of Hg accumulation rate (A, $\mu g/m^{-2}(-|-)\ yr^{-1}$), $\delta^{202}Hg$ (B, ‰), $\Delta^{199}Hg$ (C, ‰), $\Delta^{200}Hg$ (D, ‰), dust flux (E, $g/m^{-2}(-|-)\ yr^{-1}$), Hg/REE, (F, mg/g, ratio of Hg concentration in ppb to Rare-Earth-Element (REE) concentration in ppm) in the AMS peat core. Lines + Shaded fields in (B), (C) and (D) represent mean + maximum 2σ of analytical uncertainties on multiple standard materials (Supplementary information Table S1). White field (dry, high dust, SWW shifted poleward) and cyan field (wet, low dust, SWW shifted equatorward) separate the time series mainly following the dust periods established in Li et al., (2020b) (4600BCE-4200BCE, 4200BCE-3000BCE, 3000BCE-1600BCE, 1600BCE-700BCE, 700BCE-600CE, 600CE-present). Episode of 700BCE-600CE shown in gradient lines is a dust flux transition period characterized by gradual poleward displacement of the SWW (i.e. drying period with increasing dust, Li et al., 2020b). Horizontal-lines separate 600CE-1450CE, 1450CE-1900CE and post-1900CE based on the onset of large-scale Spanish mining and industrial activity. (For interpretation of the references to colour in this figure legend, the reader is referred to the web version of this article.)

2019; Donovan et al., 2013). Slightly negative $\Delta^{200}Hg$ is measured in five SH rainfall samples out of 21 (one at TDF with −0.1 ‰, and four at AMS from −0.05% to −0.01%, 2σ = 0.10%), which is in contrast to the broadly observed positive NH rainfall $\Delta^{200}Hg$. Back trajectory models show that AMS rainfall $\Delta^{200}Hg$ is significantly negatively correlated with the mean air pressure of the trajectories ($P < 0.05$, $R^2 = 0.38$, Supplementary Information Text S1 and Fig. S1), i.e. the higher the air mass altitude of a rain event, the higher the $\Delta^{200}Hg$. Similarly, there is a significantly positive relationship between TDF $\Delta^{200}Hg$ and the mixing depth of the trajectories ($P < 0.01$, $R^2 = 0.76$, Supplementary Information Fig. S2), indicating negative TDF rain $\Delta^{200}Hg$ to be mainly produced in the marine boundary layer. We suggest that negative $\Delta^{200}Hg$ in rainfall Hg^{II} from marine boundary layer trajectories at TDF and

AMS is likely produced by in-situ Hg^0 oxidation by marine halogens and retains the isotopic signatures of originated Hg^0 (Douglas and Blum, 2019), e.g., with negative $\Delta^{200}Hg$ signature.

The AMS peatland is located at a much higher elevation than the rainfall sampling point (771 m vs 55 m a.s.l.). We therefore select the $\Delta^{200}Hg$ signatures from those rainfall events with mean air pressure below 960 hPa (>450 m a.s.l.) to be included in the AMS rainfall Hg^{II} end-member. There are five AMS rainfall samples with mean trajectory air pressure below 960 hPa, which have an average $\Delta^{200}Hg$ of 0.12 ± 0.07 ‰ (1σ, n = 5). This value is similar to the mean $\Delta^{200}Hg$ signatures at the high-altitude-located MAI Observatory in Reunion Island (0.11 ‰ ± 0.04 ‰, 1σ, n = 3, 2160 m a.s.l.), and also the NH mean rainfall $\Delta^{200}Hg$ at remote sites (0.16 ‰ ± 0.07 ‰, 1σ, n = 55, Fig. 2B). We use the AMS mean rainfall $\Delta^{200}Hg$ of 0.12 ‰ for the Hg^{II} deposition end-member to the peatland, and we propose a SH mean rainfall $\Delta^{200}Hg$ of 0.08 ± 0.08 ‰ (1σ, n = 21) based on all three sites, AMS, TDF, MAI. The AMS Hg^0 $\Delta^{200}Hg$ signature of −0.06 ± 0.02 ‰ (n = 23) is used as the Hg^0 deposition end-member to the peatland.

4.2. Hg cycling in peatlands

Peatlands receive Hg mainly through plant uptake of atmospheric Hg^0 and rainfall Hg^{II} input. Plant uptake of atmospheric Hg^0 is likely followed by oxidation by reactive oxygen species or enzymes (e.g., catalase, Du and Fang, 1983; Liu et al., 2021) and the intra-cellular product Hg^{II} sequestered to thiol-carrying organic compounds. Rainfall Hg^{II} is also likely to be bind to extra-cellular thiol functional groups (Skyllberg et al., 2000). Thiol absorption of Hg^{II} is not found to cause any significant MDF (Wang et al., 2020). A two-year litter decomposition experiment shows a positive but small shift in $\delta^{202}Hg$ (−3.23 ± 0.12 ‰ to −2.93 ± 0.12 ‰, 2σ), an insignificant change in $\Delta^{199}Hg$ (−0.28 ± 0.07 ‰ to −0.34 ± 0.07 ‰, and a constant $\Delta^{200}Hg$ (−0.04 ± 0.09 ‰, 1σ, n = 8) in the residual Hg^{II} of decompositing litter (Yuan et al., 2020). This suggests an insignificant change in Hg isotope composition during litter decomposition. Similar to NH vegetation, AMS peat $\delta^{202}Hg$ (−0.66 ± 0.24 ‰, 1σ, n = 58) is lower than corresponding Hg^0 (Demers et al., 2013; Jiskra et al., 2015; Enrico et al., 2016; Yu et al., 2016; Zheng et al., 2016). It suggests the preferential uptake of light Hg isotopes by peatland vegetation, possibly related to diffusion and/or intra-cellular oxidation by enzymatic processes (Rutter et al., 2011; Zhou et al., 2021a), regardless of the vegetation species and geological substrate (Zheng et al., 2016). The shift of $\delta^{202}Hg$ from AMS Hg^0 to AMS peat (1.2 ‰) is however smaller than in other studies (e.g., 2.5 ‰ in French peat bogs, Enrico et al., 2016; >2.5 ‰ in a various vegetation types summarized in Zhou et al., 2021a). This is partly due to the contribution of Hg^{II} deposition, with positive $\delta^{202}Hg$, to AMS peat (Fig. 2).

The Hg-thiol complexes can be eventually transformed to immobile nanoparticulate mercury sulfides within the plant (Manceau et al., 2015), or possibly reduced by photochemical, microbial and/or non-photo abiotic processes, leading to partial Hg^0 evasion. Hg evasion from vegetation and organic soils is a topic of active research and debate (Agnan et al., 2016; Cooke et al., 2020; Bishop et al., 2020; Zhou et al., 2021a) due to varying magnitudes of evasion flux found in different studies. For example, Hg exchange studies indicate important net Hg^0 emission from Scandinavian peat at 64°N based on continuous flux measurement during snow-free period (May-Oct) (Osterwalder et al., 2017), moderate Hg re-emission from Scandinavian organic forest soils at 64°N based on Hg isotopic tracing approach (Jiskra et al., 2015), or temporally limited Hg^0 emission from the Alaskan permafrost tundra at 68°N based on both flux and isotope measurements (Obrist et al., 2017). Limited Hg^0 formation can also be found in the peat catotelm - a section permanently below the peat water table- due to strong binding of Hg^{II} to organic matter (Poulin et al., 2019). Other studies provide evidence that vegetation type (Rydberg et al., 2010), temperature as well as insolation (Fahnestock et al., 2019), microbial activity (Fritsche et al., 2008), and soil characteristics (Zhou et al., 2021b) influence net Hg^0 exchange.

The magnitude of Hg^0 re-emission and associated reduction processes are likely to be site-specific and closely associated with local ecology and climate. Such processes can be traced using Hg MDF and/or MIF of odd-mass isotopes. Jiskra et al., (2015) indicated for boreal organic soils how trends in $\Delta^{199}Hg/\delta^{202}Hg$ and $\Delta^{199}Hg/\Delta^{201}Hg$ ratios reflect O- and S-ligand assisted photochemical, dark abiotic, and microbial reduction. Enrico et al., (2016) observed small negative $\Delta^{199}Hg$ shifts, relative to atmospheric deposition $\Delta^{199}Hg$, in ombrotrophic peat cores from the French Pyrenees, suggesting minor photochemical re-emission of Hg at the peat surface. The AMS peat $\Delta^{199}Hg/\Delta^{201}Hg$ slope is 1.29 ± 0.10 (1σ, Fig. 4A), which is similar to the slope of 1.19 in the French peat cores (Enrico et al., 2017). Both these two peat $\Delta^{199}Hg/\Delta^{201}Hg$ slopes are significantly higher than the SH and NH atmospheric Hg slopes of 1.0 (R^2 = 0.92, p < 0.001, Fig. 4A) and 0.92 (Supplementary Information Fig. S3), respectively, which indicate a magnetic isotope effect similar to Hg^{II} photoreduction reactions in the presence of natural organic matter ($\Delta^{199}Hg/\Delta^{201}Hg$ ratio of 1.0 ± 0.01, 1σ, Blum and Bergquist, 2007).

Peat $\Delta^{199}Hg$ during pre-1900CE periods shows negligible to a small positive shift from the theoretical $\Delta^{199}Hg$ based on peat $\Delta^{200}Hg$ and conservative mixing of atmospheric end-members (Fig. 4B). The positive shift of $\Delta^{199}Hg$ is compatible with enhanced photochemical MIF, via the (+)magnetic isotope effect (MIE) mechanism operating during aqueous Hg^{II} photoreduction in the presence of organic oxygen-containing ligands (Fig. 4B). We find that the magnitude of $\Delta^{199}Hg$ shift is positively correlated with $\Delta^{199}Hg$ itself (R^2 = 0.82, P < 0.001, Supplementary Information Fig. S4), indicating that during enhanced Hg^{II} wet deposition periods with higher $\Delta^{199}Hg$, the (+)MIE is dominant. This is consistent with observed (+)MIE during Hg photoreduction in rainfall (Fu et al., 2021), suggesting that the Hg^{II}-DOC complexes in rainfall (Yang et al., 2019) lead to (+)MIE during and after deposition during pre-1900CE periods.

From pre-1900CE to 20th century (1906CE-1988CE), AMS peat $\Delta^{199}Hg$ shows a negative shift by −0.25 ‰, which is opposite to the ones found in NH lake sediments (+0.23 ‰ shift, Kurz et al., 2019; +0.08 ‰ to +0.30 ‰, Lepak et al., 2020), in SH lake sediment (+0.23 ‰ to +0.34 ‰, Cooke et al., 2013; +0.23 ‰, Jiskra et al., 2022) and in NH peat records (+0.13 ‰ to +0.30 ‰, Enrico et al., 2017). The opposite shift in $\Delta^{199}Hg$ between AMS peat and other global archives suggests a significant change in the post-depositional process on deposited anthropogenic Hg in 20th century, enabling negative $\Delta^{199}Hg$ and (−)MIF to be observed in AMS peat. Negatively-shifted $\Delta^{199}Hg$ in association with the corresponding $\Delta^{199}Hg/\Delta^{201}Hg$ slope of 1.55 ± 0.44 (1σ) is not in line with the process of foliar Hg^{II} photoreduction, which produces a $\Delta^{199}Hg/\Delta^{201}Hg$ slope of 0.79 ± 0.06 (Yuan et al., 2019). Rather, negatively-shift $\Delta^{199}Hg$ in 20th century is likely driven by nuclear volume fractionation, possibly via dark abiotic Hg reduction (negative $\Delta^{199}Hg$ in residual Hg^{II} and $\Delta^{199}Hg/\Delta^{201}Hg$ ratio of 1.6, Zheng and Hintelmann, 2010). Similar findings are also made in Yuan et al., (2020), who show a $\Delta^{199}Hg/\Delta^{201}Hg$ slope of 1.36 ± 0.28 with negative $\Delta^{199}Hg$ in a forest organic soil profile (1603–2002CE) and suggests dark abiotic reduction of Hg^{II} as the most probable mechanism. Even though different Hg reduction mechanisms with variable odd-MIF in our study may suggest minor post-depositional odd-MIF in the AMS peat core, peat $\Delta^{199}Hg$ and $\Delta^{200}Hg$ are overall significantly correlated along the Hg^0 and Hg^{II} deposition end-member mixing line (R^2 = 0.67, P < 0.001, n = 58, supplementary

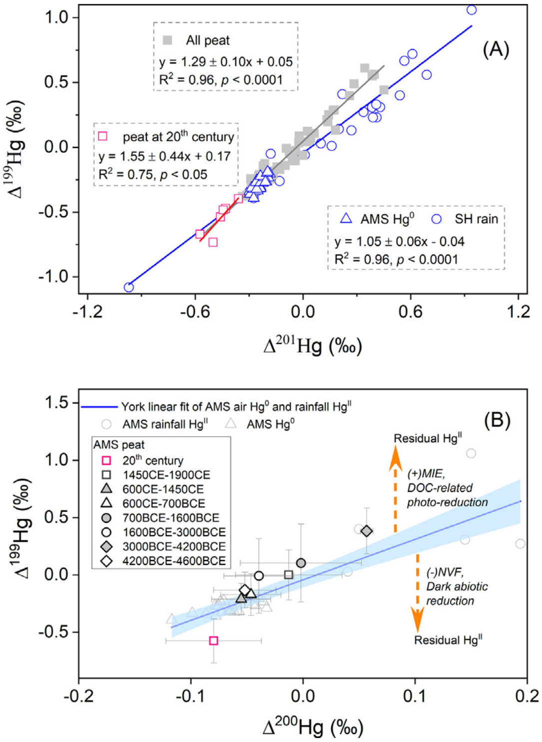

Fig. 4. (A) Δ^{199}Hg vs Δ^{201}Hg in the whole peat core (grey full squares), in peat in 20th century (1906CE-1988CE, pink open squares), AMS Hg^0 (blue open triangles) and SH rainfall Hg^{II} (blue open circles). Lines represent York linear regression in Hg^0 and rainfall (blue), the whole peat core (grey) and 20th century peat samples (red). (B) Δ^{199}Hg vs Δ^{200}Hg in AMS rainfall Hg^{II} (grey open circles), Hg^0 (grey open triangles) and peat (pink squares: 20th century, open squares: 1450CE-1900CE, full triangles: 600CE-1900CE, open triangles: 700BCE-600CE, full dots: 1600BCE-700BCE, open dots: 3000BCE-1600BCE, full diamonds: 4200BCE-3000BCE, open diamonds: 4600BCE-4200BCE). Blue line represents a York linear regression of AMS Hg^0 and rainfall Hg^{II} end-members with considering 2σ analytical uncertainties. Upward orange dash arrow stands for the trajectory of residual Hg^{II} under aqueous photoreduction of Hg^{II} in presence of dissolved organic matter (DOC) with (+) Magnetic Isotope Fractionation (MIE), while downward orange dash arrow represents dark reduction by natural organic matter under (−) nuclear volume effect. (For interpretation of the references to colour in this figure legend, the reader is referred to the web version of this article.)

Fig. S5; Fig. 4b). This suggests that peat Δ^{199}Hg and Δ^{200}Hg variability is mostly driven by the Hg deposition sources, i.e. variable Hg^0 plant uptake as well as Hg^{II} wet and dry deposition.

4.3. Peat Δ^{200}Hg reconstruction of Hg^0 uptake and Hg^{II} deposition

Most AMS peat Hg MIF resembles Hg^0 MIF signatures (Fig. 2A; 2B). This indicates that vegetation uptake of Hg^0 is an important source of Hg to AMS peat. We reconstructed peat dry HgAR (Hg^0AR, i.e. plant Hg^0 uptake, Fig. 5A) and wet HgAR (Hg^{II}AR, Fig. 5B), by making use of total peat HgAR, and the Δ^{200}Hg mass balance with equations (4) and (5). We find that, on average, plant Hg^0 uptake dominated Holocene Hg sequestration in AMS peat (>80%). Vegetation Hg^0 uptake as dominant Hg pathway to AMS peat is consistent with the findings in Pyrenean peatlands (Enrico et al., 2016).

Both Δ^{199}Hg and Δ^{200}Hg display higher values at 4200BCE-3000BCE (Δ^{199}Hg = 0.38 ± 0.14 ‰, Δ^{200}Hg = 0.06 ± 0.01 ‰, 1σ, n = 3) and 1600BCE-700BCE (Δ^{199}Hg = 0.10 ± 0.34 ‰, Δ^{200}Hg = 0.00 ± 0.05 ‰, 1σ, n = 6), than during other pre-1450CE periods (Δ^{199}Hg = −0.08 ± 0.23 ‰, Δ^{200}Hg = −0.04 ± 0.03 ‰, 1σ, n = 41, Fig. 3C; 3D). These two periods with high values of Δ^{199}Hg and Δ^{200}Hg lie closer to the AMS rainfall Hg isotope end-member, and likely correspond to periods of enhanced rainfall, also inferred from Rare-Earth-Element (REE)-based dust proxies (Li et al., 2020b). Both Δ^{199}Hg and Δ^{200}Hg are significantly correlated with dust flux prior to 1450CE ($R^2_\Delta^{199}$Hg-dust = 0.25, $P < 0.001$; $R^2_\Delta^{200}$Hg-dust = 0.29, $P < 0.001$, 2-tailed test of significance). Higher peat Hg^0AR is observed during the dry, high dust periods (3000BCE-1600BCE and 700BCE-600CE) than during other pre-1450CE wetter, low dust periods (Fig. 5A).

4.4. Role of dust deposition and climate on peat Hg accumulation

Prior to 1450CE, when Hg deposition to the peatlands was dominated by natural origins (Amos et al., 2015), AMS HgAR are significantly correlated with REE-based dust flux (Fig. 3E, $P < 0.001$, $R^2 = 0.64$, 2-tailed test of significance). Peat Hg/REE varies from 23 to 273 mg g^{-1}, which is much higher than the Hg/REE ratio of 0.38 mg g^{-1} in the crustal dust ($Crust_{Hg}$ = 56 ng g^{-1}, and $Crust_{REE}$ = 148 μg g^{-1}, Rudnick et al., 2003). This indicates that a direct Hg contribution from natural atmospheric mineral dust to peat is negligible. Low ash content in AMS peat profile (<3% in the whole profile, Supplementary Information Table S5) further suggests that Hg in mineral dust is unlikely a significant Hg source to peat. Hg/REE increases at 3000BCE-1600BCE and 700BCE-600CE (Fig. 3F; Supplementary Information Table S5), where enhanced dust flux and enhanced Hg^0AR are observed (Fig. 5). This suggests an indirect influence of dust on bog vegetation Hg^0 uptake, via changes in regional or even hemispheric marine productivity and its influence on atmospheric Hg^0 levels, peat primary productivity, or peat bog ecology.

High dust, high Hg^0AR periods of 3000BCE-1600BCE and 700BCE-600CE correspond to poleward-shifted SWW, which is the "austral summer-like" climate pattern with warmer Southern Ocean surface (Metzl et al., 2006) and stronger solar radiation. The poleward-shifted SWW during these periods can potentially enhance the upwelling of Hg-rich deep waters in the Southern Ocean by intensifying the Antarctic Circumpolar Current (Bentley et al., 2009). High Hg^0AR periods of 3000BCE-1600BCE and 700BCE-600CE coincide with higher marine productivity in Southern subtropical waters inferred from the foraminiferal productivity index in two marine cores from the same sector as AMS (H214 core in Samson et al., 2005; MD97-2121 in Marr et al., 2013; Bostock et al., 2019). During modern austral summer, the oceanic region located southwest of AMS is highly productive (Angot et al., 2014). It seems to be reasonable to speculate that high Hg^0AR at 3000BCE-1600BCE and 700BCE-600CE can be attributed to elevated atmospheric Hg^0 levels from warmer or more productive SH ocean regions, which are major sources for SH atmospheric Hg^0 (Vandal et al., 1993; Bieser et al., 2020). The reduction of surface oceanic Hg^{II} to Hg^0 can be mediated by solar radiation (Soerensen et al., 2010), marine biota (Fitzgerald et al., 1984), and organic compounds (Soerensen et al., 2013). Despite these deductions, modern qualified Hg^0 observational data at AMS (2012–2021 time period) shows no seasonality with no statistically distinguishable Hg^0 concentrations in austral winter (1.07 ng m^{-3}) and summer (1.05 ng m^{-3}) (Magand and Dommergue, 2021), arguing against a strong link between marine Hg^0 emission and peat Hg^0AR.

A more likely explanation for enhanced peat Hg^0AR at 3000BCE-1600BCE and 700BCE-600CE is an increase in peat primary productivity. Higher atmospheric dust deposition can enhance the fertilization of the peatland through more nutrient inputs and then promote peat vegetation primary productivity (Kylander et al., 2018). High primary productivity will increase annual peat Hg^0 sequestration per surface area (in μg m^{-2}) due to the additional biomass production. The net peat accumulation rate (g m^{-2} yr^{-1}) at AMS, i.e. a combination of synchronous changes in the primary productivity and decomposition rate, is not significantly different

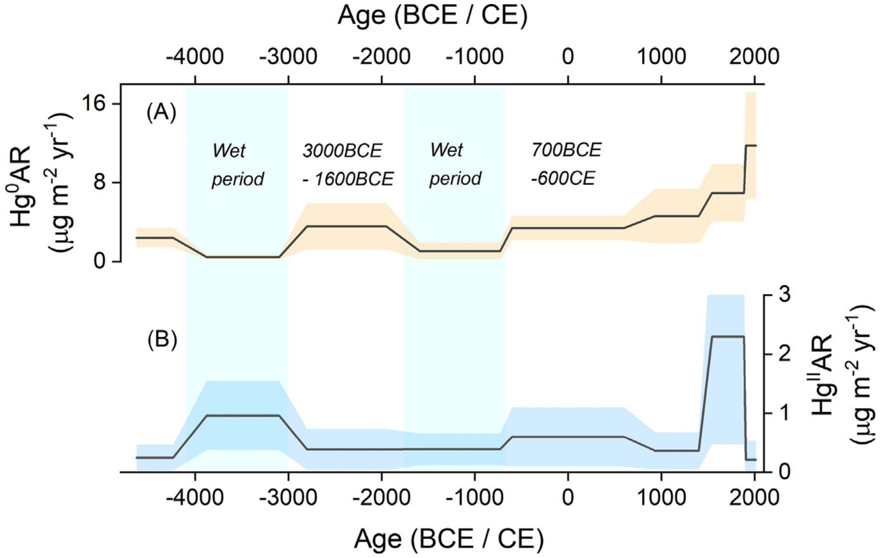

Fig. 5. Temporal profile of (A) reconstructed Hg dry deposition (Hg^0AR, $\mu g/m^{-2}(-|-)$ yr^{-1}, mean + 1σ) and (B) reconstructed Hg wet deposition ($Hg^{II}AR$, $\mu g/m^{-2}(-|-)$ yr^{-1}, mean + 1σ). High dust periods of 3000BCE-1600BCE and 700BCE-600CE are indicated in Fig. 3.

at 3000BCE-1600BCE and 700BCE-600CE from the corresponding previous periods ($P > 0.05$ for both, two sided t-test), based on the age model derived from 20 radiocarbon-dated sections (Li et al., 2020b). We therefore assume a synchronous higher primary productivity (discussed above) and higher decomposition rate at 3000BCE-1600BCE and 700BCE-600CE. The assumption of higher decomposition can be supported by a relatively dry climate during these two intervals inferred from dust proxies, where more dust input at AMS results from less wind and less humidity. Relatively dry climate lowers the peatland water table, which enhances the dominant aerobic decay in the peatland (i.e. high decomposition, Clymo, 1984; Young et al., 2019). Increased peat Hg accumulation and high decomposition likely occur synchronously during high dust and humidity regime, leading to enhanced net peat Hg^0AR. In summary, variability in AMS peat Hg deposition prior to 1450CE appears to be mainly driven by changes in SWW-driven peatland vegetation primary productivity, and less likely by changes in marine Hg^0 evasion and SH Hg^0 levels.

4.5. Qualitative and quantitative rainfall reconstruction from an isotopic perspective

A recent SH Holocene Hg isotope record in lake Titicaca sediment shows a strong link between deposited $\Delta^{200}Hg$ and paleo-rainfall, suggesting temporal variation of $\Delta^{200}Hg$ in archives could reflect a change in rainfall rates prior to industrialization (Jiskra et al., 2022). AMS $\Delta^{200}Hg$ variability follows the trend of dust flux profile, a qualitative proxy for SWW (Fig. 6A; 6B). This highlights the potential of using $\Delta^{200}Hg$ as a qualitative rainfall proxy. Above we used a binary isotope mixing model based on distinct $\Delta^{200}Hg$ signatures in both atmospheric end-members (i.e. Hg^0 and rainfall Hg^{II}, equations (3) and (4)), to estimate past Hg^0AR and $Hg^{II}AR$. Here we take this approach a step further to try and estimate Holocene rainfall rate, by making use of the relationship between modern rainfall and Hg^{II} wet deposition. Modern Hg^{II} wet deposition has been enhanced by anthropogenic Hg emission, which should be considered in any rainfall reconstruction model. To present different possibilities of using $Hg^{II}AR$ and $\Delta^{200}Hg$ signatures to estimates the Holocene rainfall, we propose two models under different assumptions (Model 1 & Model 2).

Model 1 is free from the effects of anthropogenic Hg input and peat Hg re-emission rates by making use of the $\Delta^{200}Hg$ compositions in atmospheric end-members, deposited $Hg^{II}AR$, and deposited Hg^0AR (Supplementary Information Text S2 and equations S1 to S6 with detailed assumptions). Briefly, it assumes that (i) rainfall Hg^{II} concentration and atmospheric Hg^0 are proportional at all times, (ii) peat Hg re-emission does not discriminate between the original deposition source (Hg^{II} vs Hg^0), and (iii) the peat vegetation uptake rate (cm s^{-1}) of gaseous Hg^0 was constant over time. In other words, the variations in Hg^{II}/Hg^0 accumulation (and thus peat $\Delta^{200}Hg$) are exclusively the result of variable rainfall rates. The rainfall profile estimated from Model 1 follows the trends of dust flux and peat $\Delta^{200}Hg$ (Fig. 6A; 6C, details please see Supplementary Information Text S2).

Model 2 is based on the relationship between Hg^{II} wet deposition and rainfall in modern AMS observations, which shows that AMS daily rainfall volume from 2013 to 2014 is significantly correlated with the associated Hg wet deposition rate (ng m^{-2} d^{-1}, $P < 0.01$, $R^2 = 0.53$, Supplementary Information Fig. S6). We extend this daily relationship to the annual scale by multiplying with a factor of 365 (Supplementary Information Text S3 and equation S7). Modern Hg wet deposition (post 1990CE), is however strongly influenced by the x3 anthropogenic enrichment of SH atmospheric Hg relative to pre-1450CE and x2.5 relative to 1450CE-1880CE, respectively (Li et al., 2020a). To translate Holocene peat $Hg^{II}AR$ into rainfall rate, we therefore correct reconstructed peat $Hg^{II}AR$ by a factor of 3 and 2.5 for pre-1450CE $Hg^{II}AR$ and 1450CE-1900CE $Hg^{II}AR$, respectively (Supplementary Information equations S8 and S9). No correction for Hg re-emission from peat is made in Model 2, i.e. we assume that reconstructed $Hg^{II}AR$ is equal to Hg^{II} wet deposition. This assumption implies that either peat Hg re-emission was small, or that it was significant, but proportional to the Hg deposition rate. This assumption is based on (i) the broadly consistent anthropogenic Hg enrichment factors between sediment and peat in both hemispheres (13 vs 16 in the NH and 4 vs 6 in the SH, Li et al., 2020a), and (ii) the reconstructed 2001CE-2014CE rainfall of 840 mm yr^{-1} (median, 570–1060 mm yr^{-1}, interquartile range), is in good agreement with observed rainfall at AMS with 833 mm yr^{-1} in 2013 and 864 mm yr^{-1} in 2014 (Sprovieri et al., 2017). The reconstructed Holocene rainfall rates broadly follow the trend of the qualitative SWW strength profile

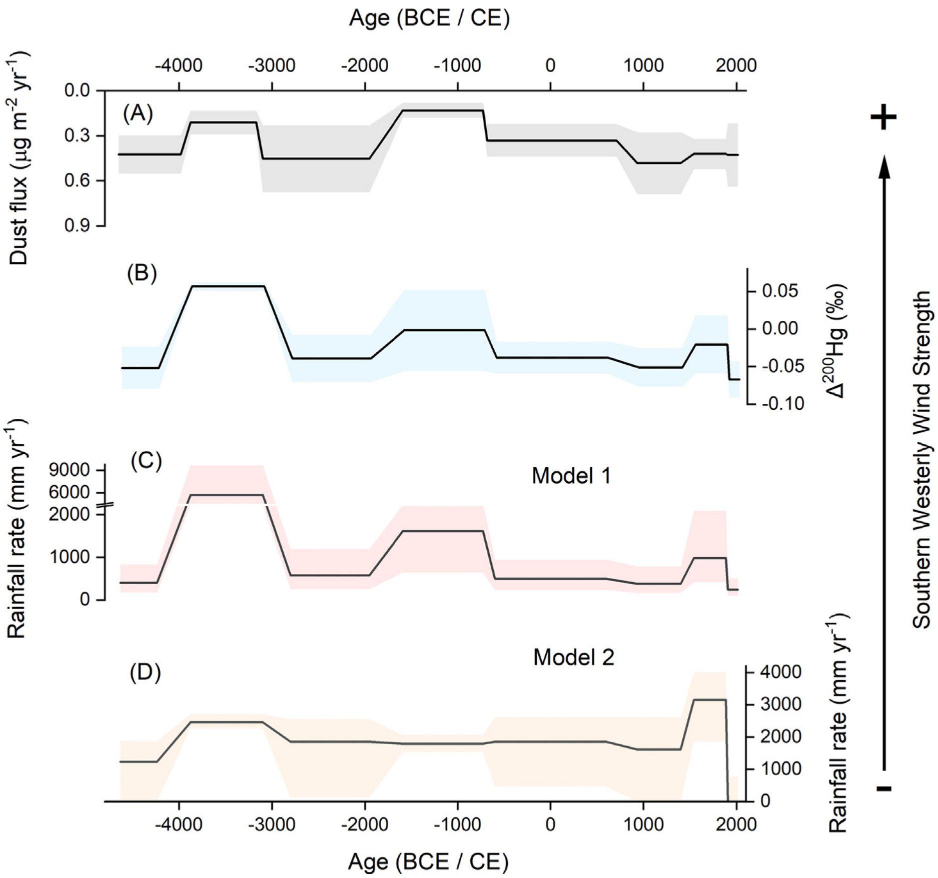

Fig. 6. Profiles of (A) dust flux (reversed scale in Y axis, μg/m^{-2}(–|–) yr^{-1}, mean + 1σ), (B) Δ^{200}Hg (‰, mean + 1σ), (C) Δ^{200}Hg-based reconstructed rainfall rate using Model 1 under Monte Carlo simulation (mm yr^{-1}, median + interquartile), and (D) Δ^{200}Hg-based reconstructed rainfall rate using Model 2 under Monte Carlo simulation (mm yr^{-1}, median + interquartile). The strength of the Southern Westerly Winds is shown in "+" and "−", which is indicated by the dust flux variation (Li et al., 2020b).

inferred from the dust flux (Fig. 6A; 6D). The discrepancy of reconstructed rainfall rates between Model 2 and dust proxies at 1600BCE-700BCE highlights the need for further investigations on the model methods (e.g., potential Hg re-emission) and/or cross-validation using other climate indicators (e.g., plant macrofossil, testate amoebae).

Both models capture the broad trend of SWW dynamics inferred from the dust deposition proxy (Fig. 6), even though model results show different quantitative rainfall rates for the same periods. These differences in the rainfall estimates can be attributed to their distinct assumptions and methods (e.g., re-emission rates, adjustment on anthropogenic Hg input and constant uptake rate of gaseous Hg^0). For example, the high rainfall rate estimate of 5700 mm yr^{-1} for 4200BCE-3000BCE in Model 2 is a consequence of the assumed constant uptake rate of gaseous Hg^0 (see Supplementary Information Text S3). Although neither of these two models is perfect, they each have their strengths in estimating rainfall from peat Hg isotopes. Model 1 allows a variable uptake rate of gaseous Hg^0, while Model 2 is independent from re-emission rates and anthropogenic enrichment factors. Overall, our findings highlight the potential of using Hg stable isotopes to reconstruct the paleo-rainfall patterns as well as to trace Hg sources and post-depositional processes.

4.6. Implications

The Amsterdam Island peatland is an ideal location to document the temporal changes in SH atmospheric Hg deposition and its relation to climate due to its remote location and two main ways of Hg sequestration in peat via vegetation uptake of Hg^0 and rainfall supply of Hg^{II}. Coherent changes in Amsterdam Island peat Hg accumulation rate, dust deposition rate, odd MIF and even MIF reflect changes in Holocene SWW dynamics. Poleward shifted SWW lead to drier, warmer climate conditions at the Amsterdam Island, where higher continental dust deposition provides nutrients that stimulate peatland primary production and concomitant bog vegetation Hg^0 uptake. MDF and odd MIF of Hg isotopes enable us to evaluate Hg cycling upon its deposition to the peatland (e.g., potential mobility), while even MIF allows us to reconstruct the two main Hg deposition pathways (i.e. dry and wet deposition). Even MIF further shows its potential as a qualitative and semi-quantitative paleo rainfall proxy. To establish Hg isotopes as a robust climate indicator or post-depositional process tracer in peatland, more investigations are still needed on the mechanisms of Hg cycling in the atmospheric sources (e.g., MDF and MIF under Hg oxidation within and above marine boundary layers) and in the peatland with not only one but multiple cores (e.g., MDF and MIF during uptake of Hg^0 among different plant species). Presently, we suggest that Hg stable isotopes in peat records can at least be used as a qualitative climate proxy identifying dry and wet periods. A better understanding of peat Hg cycling and associated isotope fractionation, together with a better characterization of rainfall isotope signatures, might allow for quantitative reconstructions.

Data availability

The data supporting the findings of this study are provided in the article and Supplementary Material.

Declaration of Competing Interest

The authors declare that they have no known competing financial interests or personal relationships that could have appeared to influence the work reported in this paper.

Acknowledgements

We deeply thank all overwintering staff at AMS and the French Polar Institute Paul-Emile Victor (IPEV) staff and scientists who helped with the setup and maintenance of the experiment at AMS in the framework of the GMOStral-1028 IPEV program as well as the support they provided during the 1066 PARAD field campaign. We acknowledge OPAR (Observatoire de Physique de l'Atmosphère à La Réunion), funded by CNRS-INSU and Université de La Réunion and managed by OSU-R (Observatoire des Sciences de l'Univers à La Réunion, UMS 3365). We thank the NOAA Air Resources Laboratory (ARL) for providing the HYSPLIT transport and dispersion model and the READY website (https://www.ready.noaa.gov). We are deeply grateful for Andrea Coronato and Ramiro López from CADIC-CONICET (Ushuaia), Kayne Dipilato and Pablo DéAntueno for their incredible efforts on rainfall sampling and coordination in Tierra del Fuego. We appreciate the great efforts from Jérôme Chmeleff and Laure Laffont for their maintenance on the analytical machines MC-ICPMS and DMA-80, respectively. Amsterdam Island Hg0 data, accessible in GMOS-FR national data portal (https://gmos.aeris-data.fr/) were collected via instruments coordinated by the IGE-PTICHA technical platform dedicated to atmospheric chemistry field instrumentation and maintained by the French national center for Atmospheric data and services AERIS, which is acknowledged by the authors. Amsterdam Island Hg0 data are funded by the European Union 7th Framework Programme project Global Mercury Observation System (GMOS 2010-2015, Nr. 26511 to O.M.), the GMOStral-1028 IPEV program since 2012 (to O.M.), and the French national LEFE-CHAT CNRS/INSU program (TOPMMODEL project, Nr. AO2017-984931 to O.M.). We thank the China Scholarship Council for supporting C. Li's PhD work (Nr. 201506990002). Field work was partially funded by the French Polar Institute (IPEV, Brest, France) through the IPEV Programmes 1066 "PARAD" to F.D.V.. J.E.S. and O.M. acknowledge funding from the H2020 ERA-PLANET iGOSP and iCUPE programs (Nr. 689443). We thank three anonymous reviewers for their time and very helpful comments.

Appendix A. Supplementary material

All primary research data generated from this study are provided in the Supplementary Materials. Supplementary material to this article can be found online at https://doi.org/10.1016/j.gca.2022.11.024.

References

Agnan, Y., Le Dantec, T., Moore, C.W., Edwards, G.C., Obrist, D., 2016. New Constraints on Terrestrial Surface-Atmosphere Fluxes of Gaseous Elemental Mercury Using a Global Database. Environ. Sci. Technol. 50, 507–524.

Amos, H.M., Sonke, J.E., Obrist, D., Robins, N., Hagan, N., Horowitz, H.M., Mason, R.P., Witt, M., Hedgecock, I.M., Corbitt, E.S., Sunderland, E.M., 2015. Observational and Modeling Constraints on Global Anthropogenic Enrichment of Mercury. Environ. Sci. Technol. 49, 4036–4047.

Angot, H., Barret, M., Magand, O., Ramonet, M., Dommergue, A., 2014. A 2-year record of atmospheric mercury species at a background Southern Hemisphere station on Amsterdam Island. Atmos. Chem. Phys. 14, 11461–11473.

Bentley, M.J., Hodgson, D.A., Smith, J.A., Cofaigh, C.Ó., Domack, E.W., Larter, R.D., Roberts, S.J., Brachfeld, S., Leventer, A., Hjort, C., Hillenbrand, C.-D., Evans, J., 2009. Mechanisms of Holocene palaeoenvironmental change in the Antarctic Peninsula region. The Holocene 19, 51–69.

Bieser, J., Angot, H., Slemr, F., Martin, L., 2020. Atmospheric mercury in the Southern Hemisphere – Part 2: Source apportionment analysis at Cape Point station, South Africa. Atmos. Chem. Phys. 20, 10427–10439.

Bishop, K., Shanley, J.B., Riscassi, A., de Wit, H.A., Eklöf, K., Meng, B., Mitchell, C., Osterwalder, S., Schuster, P.F., Webster, J., Zhu, W., 2020. Recent advances in understanding and measurement of mercury in the environment: Terrestrial Hg cycling. Sci. Total Environ. 721, 137647.

Blum, J.D., Bergquist, B.A., 2007. Reporting of variations in the natural isotopic composition of mercury. Anal. Bioanal. Chem. 388, 353–359.

Blum, J.D., Sherman, L.S., Johnson, M.W., 2014. Mercury Isotopes in Earth and Environmental Sciences. Annu. Rev. Earth Planet. Sci. 42, 249–269.

Bostock, H.C., Prebble, J.G., Cortese, G., Hayward, B., Calvo, E., Quirós-Collazos, L., Kienast, M., Kim, K., 2019. Paleoproductivity in the SW Pacific Ocean During the Early Holocene Climatic Optimum. Paleoceanogr. Paleoclimatol. 34, 580–599.

Chen, J., Hintelmann, H., Feng, X., Dimock, B., 2012. Unusual fractionation of both odd and even mercury isotopes in precipitation from Peterborough, ON, Canada. Geochim. Cosmochim. Acta 90, 33–46.

Clymo, R.S., 1984. The limits to peat bog growth. Phil. Trans. R. Soc. Lond. B 303, 605–654.

Cooke, C.A., Hintelmann, H., Ague, J.J., Burger, R., Biester, H., Sachs, J.P., Engstrom, D.R., 2013. Use and Legacy of Mercury in the Andes. Environ. Sci. Technol. 47, 4181–4188.

Cooke, C.A., Martínez-Cortizas, A., Bindler, R., Gustin, M.S., 2020. Environmental archives of atmospheric Hg deposition–A review. Sci. Total Environ. 709, 134800.

Demers, J.D., Blum, J.D., Zak, D.R., 2013. Mercury isotopes in a forested ecosystem: Implications for air-surface exchange dynamics and the global mercury cycle: MERCURY ISOTOPES IN A FORESTED ECOSYSTEM. Global Biogeochem. Cycles 27, 222–238.

Demers, J.D., Sherman, L.S., Blum, J.D., Marsik, F.J., Dvonch, J.T., 2015. Coupling atmospheric mercury isotope ratios and meteorology to identify sources of mercury impacting a coastal urban-industrial region near Pensacola, Florida, USA: ATMOSPHERIC MERCURY ISOTOPE RATIOS. Global Biogeochem. Cycles 29, 1689–1705.

Donovan, P.M., Blum, J.D., Yee, D., Gehrke, G.E., Singer, M.B., 2013. An isotopic record of mercury in San Francisco Bay sediment. Chem. Geol. 349–350, 87–98.

Doucet, S., Weis, D., Scoates, J.S., Debaille, V., Giret, A., 2004. Geochemical and Hf–Pb–Sr–Nd isotopic constraints on the origin of the Amsterdam–St. Paul (Indian Ocean) hotspot basalts. Earth Planet. Sci. Lett. 218, 179–195.

Douglas, T.A., Blum, J.D., 2019. Mercury Isotopes Reveal Atmospheric Gaseous Mercury Deposition Directly to the Arctic Coastal Snowpack. Environ. Sci. Technol. Lett. 6, 235–242.

Du, S.-H., Fang, S.C., 1983. Catalase activity of C3 and C4 species and its relationship to mercury vapor uptake. Environ. Exp. Bot. 23, 347–353.

Enrico, M., Roux, G.L., Marusczak, N., Heimbürger, L.-E., Claustres, A., Fu, X., Sun, R., Sonke, J.E., 2016. Atmospheric Mercury Transfer to Peat Bogs Dominated by Gaseous Elemental Mercury Dry Deposition. Environ. Sci. Technol. 50, 2405–2412.

Enrico, M., Le Roux, G., Heimbürger, L.-E., Van Beek, P., Souhaut, M., Chmeleff, J., Sonke, J.E., 2017. Holocene Atmospheric Mercury Levels Reconstructed from Peat Bog Mercury Stable Isotopes. Environ. Sci. Technol. 51, 5899–5906.

Estrade, N., Carignan, J., Sonke, J.E., Donard, O.F.X., 2009. Mercury isotope fractionation during liquid–vapor evaporation experiments. Geochim. Cosmochim. Acta 73, 2693–2711.

Fahnestock, M.F., Bryce, J.G., McCalley, C.K., Montesdeoca, M., Bai, S., Li, Y., Driscoll, C.T., Crill, P.M., Rich, V.I., Varner, R.K., 2019. Mercury reallocation in thawing subarctic peatlands. Geochem. Persp. Let., 33–38

Fitzgerald, W.F., Gill, G.A., Kim, J.P., 1984. An Equatorial Pacific Ocean Source of Atmospheric Mercury. Science 224, 597–599.

Fitzgerald, W.F., Lamborg, C.H., 2003. Geochemistry of mercury in the environment. In: Lollar, B.S. (Ed.), Treatise on Geochemistry. Elsevier, New York, pp. 107–148.

Frenot, Y., Valleix, T., 1990. Notice de la carte des sols de l'ile Amsterdam: terres Australes et Antarctiques Françaises.

Fu, X., Marusczak, N., Wang, X., Gheusi, F., Sonke, J.E., 2016a. Isotopic Composition of Gaseous Elemental Mercury in the Free Tropospshere of the Pic du Midi Observatory, France. Environ. Sci. Technol. 50, 5641–5650.

Fu, X., Zhu, W., Zhang, H., Sommar, J., Yu, B., Yang, X., Wang, X., Lin, C.-J., Feng, X., 2016b. Depletion of atmospheric gaseous elemental mercury by plant uptake at Mt. Changbai, Northeast China. Atmos. Chem. Phys. 16, 12861–12873.

Fu, X., Yang, X., Tan, Q., Ming, L., Lin, T., Lin, C.-J., Li, X., Feng, X., 2018. Isotopic Composition of Gaseous Elemental Mercury in the Marine Boundary Layer of East China Sea. J. Geophys. Res. Atmos.

Fritsche, J., Obrist, D., Alewell, C., 2008. Evidence of microbial control of Hg0 emissions from uncontaminated terrestrial soils. J. Soil Sci. Plant Nutr. 171, 200–209.

Fu, X., Jiskra, M., Yang, X., Marusczak, N., Enrico, M., Chmeleff, J., Heimbürger-Boavida, L.-E., Gheusi, F., Sonke, J.E., 2021. Mass-Independent Fractionation of Even and Odd Mercury Isotopes during Atmospheric Mercury Redox Reactions. Environ. Sci. Technol. 55, 10164–10174.

Gentès, S., Maury-Brachet, R., Feng, C., Pedrero, Z., Tessier, E., Legeay, A., Mesmer-Dudons, N., Baudrimont, M., Maurice, L., Amouroux, D., Gonzalez, P., 2015. Specific Effects of Dietary Methylmercury and Inorganic Mercury in Zebrafish (*Danio rerio*) Determined by Genetic, Histological, and Metallothionein Responses. Environ. Sci. Technol. 49, 14560–14569.

Ghosh, S., Xu, Y., Humayun, M., Odom, L., 2008. Mass-independent fractionation of mercury isotopes in the environment: FRACTIONATION OF MERCURY ISOTOPES. Geochem. Geophys. Geosyst. 9, Q03004.

Gleason, J.D., Blum, J.D., Moore, T.C., Polyak, L., Jakobsson, M., Meyers, P.A., Biswas, A., 2017. Sources and cycling of mercury in the paleo Arctic Ocean from Hg stable isotope variations in Eocene and Quaternary sediments. Geochim. Cosmochim. Acta 197, 245–262.

Gratz, L.E., Keeler, G.J., Blum, J.D., Sherman, L.S., 2010. Isotopic Composition and Fractionation of Mercury in Great Lakes Precipitation and Ambient Air. Environ. Sci. Technol. 44, 7764–7770.

Horowitz, H.M., Jacob, D.J., Zhang, Y., Dibble, T.S., Slemr, F., Amos, H.M., Schmidt, J.A., Corbitt, E.S., Marais, E.A., Sunderland, E.M., 2017. A new mechanism for atmospheric mercury redox chemistry: implications for the global mercury budget. Atmos. Chem. Phys. 17, 6353–6371.

Jiskra, M., Wiederhold, J.G., Skyllberg, U., Kronberg, R.-M., Hajdas, I., Kretzschmar, R., 2015. Mercury Deposition and Re-emission Pathways in Boreal Forest Soils Investigated with Hg Isotope Signatures. Environ. Sci. Technol. 49, 7188–7196.

Jiskra, M., Sonke, J.E., Obrist, D., Bieser, J., Ebinghaus, R., Myhre, C.L., Pfaffhuber, K.A., Wängberg, I., Kyllönen, K., Worthy, D., Martin, L.G., Labuschagne, C., Mkololo, T., Ramonet, M., Magand, O., Dommergue, A., 2018. A vegetation control on seasonal variations in global atmospheric mercury concentrations. Nat. Geosci. 11, 244–250.

Jiskra, M., Sonke, J.E., Agnan, Y., Helmig, D., Obrist, D., 2019. Insights from mercury stable isotopes on terrestrial–atmosphere exchange of Hg(0) in the Arctic tundra. Biogeosciences 16, 4051–4064.

Jiskra, M., Heimbürger-Boavida, L.-E., Desgranges, M.-M., Petrova, M.V., Dufour, A., Ferreira-Araujo, B., Masbou, J., Chmeleff, J., Thyssen, M., Point, D., Sonke, J.E., 2021. Mercury stable isotopes constrain atmospheric sources to the ocean. Nature 597, 678–682.

Jiskra, M., Guédron, S., Tolu, J., Fritz, S.C., Baker, P.A., Sonke, J.E., 2022. Climatic Controls on a Holocene Mercury Stable Isotope Sediment Record of Lake Titicaca. ACS Earth Space Chem. 6, 346–357.

Jitaru, P., Gabrielli, P., Marteel, A., Plane, J.M.C., Planchon, F.A.M., Gauchard, P.-A., Ferrari, C.P., Boutron, C.F., Adams, F.C., Hong, S., Cescon, P., Barbante, C., 2009. Atmospheric depletion of mercury over Antarctica during glacial periods. Nat. Geosci. 2, 505–508.

Kritee, K., Blum, J.D., Johnson, M.W., Bergquist, B.A., Barkay, T., 2007. Mercury Stable Isotope Fractionation during Reduction of Hg(II) to Hg(0) by Mercury Resistant Microorganisms. Environ. Sci. Technol. 41, 1889–1895.

Kritee, K., Blum, J.D., Reinfelder, J.R., Barkay, T., 2013. Microbial stable isotope fractionation of mercury: A synthesis of present understanding and future directions. Chem. Geol. 336, 13–25.

Kurz, A.Y., Blum, J.D., Washburn, S.J., Baskaran, M., 2019. Changes in the mercury isotopic composition of sediments from a remote alpine lake in Wyoming, USA. Sci. Total Environ. 669, 973–982.

Kurz, A.Y., Blum, J.D., Gratz, L.E., Jaffe, D.A., 2020. Contrasting Controls on the Diel Isotopic Variation of Hg ^{0} at Two High Elevation Sites in the Western United States. Environ. Sci. Technol. 54, 10502–10513.

Kylander, M.E., Martínez-Cortizas, A., Bindler, R., Kaal, J., Sjöström, J.K., Hansson, S. V., Silva-Sánchez, N., Greenwood, S.L., Gallagher, K., Rydberg, J., Mörth, C.-M., Rauch, S., 2018. Mineral dust as a driver of carbon accumulation in northern latitudes. Sci. Rep. 8, 6876.

Lebouvier, M., Frenot, Y., 2007. Conservation and management in the French sub-Antarctic islands and surrounding seas. PPRST, 23–28.

Lepak, R.F., Janssen, S.E., Engstrom, D.R., Krabbenhoft, D.P., Tate, M.T., Yin, R., Fitzgerald, W.F., Nagorski, S.A., Hurley, J.P., 2020. Resolving Atmospheric Mercury Loading and Source Trends from Isotopic Records of Remote North American Lake Sediments. Environ. Sci. Technol. 54, 9325–9333.

Li, C., Le Roux, G., Sonke, J., Van Beek, P., Souhaut, M., Van der Putten, N., De Vleeschouwer, F., 2017. Recent 210Pb, 137Cs and 241Am accumulation in an ombrotrophic peatland from Amsterdam Island (Southern Indian Ocean). J. Environ. Radioact. 175, 164–169.

Li, C., Sonke, J.E., Le Roux, G., Piotrowska, N., Van der Putten, N., Roberts, S.J., Daley, T., Rice, E., Gehrels, R., Enrico, M., Mauquoy, D., Roland, T.P., De Vleeschouwer, F., 2020a. Unequal Anthropogenic Enrichment of Mercury in Earth's Northern and Southern Hemispheres. ACS Earth Space Chem. 4, 2073–2081.

Li, C., Sonke, J.E., Le Roux, G., Van der Putten, N., Piotrowska, N., Jeandel, C., Mattielli, N., Benoit, M., Wiggs, G.F.S., De Vleeschouwer, F., 2020b. Holocene dynamics of the southern westerly winds over the Indian Ocean inferred from a peat dust deposition record. Quat. Sci. Rev. 231, 106169.

Lindberg, S.E., Brooks, S., Lin, C.-J., Scott, K.J., Landis, M.S., Stevens, R.K., Goodsite, M., Richter, A., 2002. Dynamic Oxidation of Gaseous Mercury in the Arctic Troposphere at Polar Sunrise. Environ. Sci. Technol. 36, 1245–1256.

Liu, Y., Liu, G., Wang, Z., Guo, Y., Yin, Y., Zhang, X., Cai, Y., Jiang, G., 2021. Understanding foliar accumulation of atmospheric Hg in terrestrial vegetation: Progress and challenges. Crit. Rev. Environ., 1–22

Magand, O., Dommergue, A., 2021. Continuous measurements of atmospheric mercury at Amsterdam Island (L2). Aeris. https://.

Manceau, A., Lemouchi, C., Enescu, M., Gaillot, A.C., Lanson, M., Magnin, V., Glatzel, P., Poulin, B.A., Ryan, J.N., Aiken, G.R., Gautier-Luneau, I., 2015. Formation of mercury sulfide from Hg (II)–thiolate complexes in natural organic matter. Environ. Sci. Technol. 49, 9787–9796.

Marr, J.P., Carter, L., Bostock, H.C., Bolton, A., Smith, E., 2013. Southwest Pacific Ocean response to a warming world: Using Mg/Ca, Zn/Ca, and Mn/Ca in foraminifera to track surface ocean water masses during the last deglaciation: SW PACIFIC RESPONSE TO A WARMING WORLD. Paleoceanography 28, 347–362.

Metzl, N., Brunet, C., Jabaud-Jan, A., Poisson, A., Schauer, B., 2006. Summer and winter air–sea CO2 fluxes in the Southern Ocean. Deep-Sea Res. 53, 1548–1563.

Moody, J.L., Pszenny, A.A.P., Gaudry, A., Keene, W.C., Galloway, J.N., Polian, G., 1991. Precipitation composition and its variability in the southern Indian Ocean: Amsterdam Island, 1980–1987. J. Geophys. Res. 96, 20769.

Motta, L.C., Blum, J.D., Johnson, M.W., Umhau, B.P., Popp, B.N., Washburn, S.J., Drazen, J.C., Benitez-Nelson, C.R., Hannides, C.C.S., Close, H.G., Lamborg, C.H., 2019. Mercury Cycling in the North Pacific Subtropical Gyre as Revealed by Mercury Stable Isotope Ratios. Global Biogeochem. Cycles 33, 777–794.

Motta, L.C., Kritee, K., Blum, J.D., Tsz-Ki, T.M., Reinfelder, J.R., 2020. Mercury Isotope Fractionation during the Photochemical Reduction of Hg(II) Coordinated with Organic Ligands. J. Phys. Chem. A 124, 2842–2853.

Obrist, D., Agnan, Y., Jiskra, M., Olson, C.L., Colegrove, D.P., Hueber, J., Moore, C.W., Sonke, J.E., Helmig, D., 2017. Tundra uptake of atmospheric elemental mercury drives Arctic mercury pollution. Nature 547, 201–204.

Obrist, D., Roy, E.M., Harrison, J.L., Kwong, C.F., Munger, J.W., Moosmüller, H., Romero, C.D., Sun, S., Zhou, J., Commane, R., 2021. Previously unaccounted atmospheric mercury deposition in a midlatitude deciduous forest. Proc. Natl. Acad. Sci. USA 118. e2105477118.

Osterwalder, S., Bishop, K., Alewell, C., Fritsche, J., Laudon, H., Åkerblom, S., Nilsson, M.B., 2017. Mercury evasion from a boreal peatland shortens the timeline for recovery from legacy pollution. Sci. Rep. 7, 16022.

Outridge, P.M., Mason, R.P., Wang, F., Guerrero, S., Heimbürger-Boavida, L.E., 2018. Updated Global and Oceanic Mercury Budgets for the United Nations Global Mercury Assessment 2018. Environ. Sci. Technol. 52, 11466–11477.

Poulin, B.A., Ryan, J.N., Tate, M.T., Krabbenhoft, D.P., Hines, M.E., Barkay, T., Schaefer, J., Aiken, G.R., 2019. Geochemical Factors Controlling Dissolved Elemental Mercury and Methylmercury Formation in Alaskan Wetlands of Varying Trophic Status. Environ. Sci. Technol. 53, 6203–6213.

Rolison, J.M., Landing, W.M., Luke, W., Cohen, M., Salters, V.J.M., 2013. Isotopic composition of species-specific atmospheric Hg in a coastal environment. Chem. Geol. 336, 37–49.

Roman, H.A., Walsh, T.L., Coull, B.A., Dewailly, É., Guallar, E., Hattis, D., Mariën, K., Schwartz, J., Stern, A.H., Virtanen, J.K., Rice, G., 2011. Evaluation of the Cardiovascular Effects of Methylmercury Exposures: Current Evidence Supports Development of a Dose-Response Function for Regulatory Benefits Analysis. Environ. Health Perspect. 119, 607–614.

Rudnick, R.L., Gao, S., Holland, H.D., Turekian, K.K., 2003. Composition of the continental crust. The Crust, 4–7.

Rutter, A.P., Schauer, J.J., Shafer, M.M., Creswell, J.E., Olson, M.R., Robinson, M., Collins, R.M., Parman, A.M., Katzman, T.L., Mallek, J.L., 2011. Dry deposition of gaseous elemental mercury to plants and soils using mercury stable isotopes in a controlled environment. Atmos. Environ. 45, 848–855.

Rydberg, J., Karlsson, J., Nyman, R., Wanhatalo, I., Näthe, K., Bindler, R., 2010. Importance of vegetation type for mercury sequestration in the northern Swedish mire, Rödmossamyran. Geochim. Cosmochim. Acta 74, 7116–7126.

Samson, C.R., Sikes, E.L., Howard, W.R., 2005. Deglacial paleoceanographic history of the Bay of Plenty, New Zealand: DEGLACIAL SST BAY OF PLENTY, NEW ZEALAND. Paleoceanography 20, 1–12.

Scheuhammer, A.M., Meyer, M.W., Sandheinrich, M.B., Murray, M.W., 2007. Effects of environmental methylmercury on the health of wild birds, mammals, and fish. Ambio, 12–18.

Sherman, L.S., Blum, J.D., Johnson, K.P., Keeler, G.J., Barres, J.A., Douglas, T.A., 2010. Mass-independent fractionation of mercury isotopes in Arctic snow driven by sunlight. Nat. Geosci. 3, 173–177.

Sherman, L.S., Blum, J.D., Keeler, G.J., Demers, J.D., Dvonch, J.T., 2012. Investigation of Local Mercury Deposition from a Coal-Fired Power Plant Using Mercury Isotopes. Environ. Sci. Technol. 46, 382–390.

Sherman, L.S., Blum, J.D., Dvonch, J.T., Gratz, L.E., Landis, M.S., 2015. The use of Pb, Sr, and Hg isotopes in Great Lakes precipitation as a tool for pollution source attribution. Sci. Total Environ. 502, 362–374.

Shi, W., Feng, X., Zhang, G., Ming, L., Yin, R., Zhao, Z., Wang, J., 2011. High-precision measurement of mercury isotope ratios of atmospheric deposition over the past 150 years recorded in a peat core taken from Hongyuan, Sichuan Province. China. *Chin. Sci. Bull.* 56, 877–882.

Sial, A.N., Chen, J., Lacerda, L.D., Frei, R., Tewari, V.C., Pandit, M.K., Gaucher, C., Ferreira, V.P., Cirilli, S., Peralta, S., Korte, C., Barbosa, J.A., Pereira, N.S., 2016. Mercury enrichment and Hg isotopes in Cretaceous-Paleogene boundary successions: Links to volcanism and palaeoenvironmental impacts. Cretaceous Res. 66, 60–81.

Skyllberg, U., Xia, K., Bloom, P.R., Nater, E.A., Bleam, W.F., 2000. Binding of Mercury (II) to Reduced Sulfur in Soil Organic Matter along Upland-Peat Soil Transects. J. Environ. Qual. 29, 855–865.

Slemr, F., Angot, H., Dommergue, A., Magand, O., Barret, M., Weigelt, A., Ebinghaus, R., Brunke, E.-G., Pfaffhuber, K.A., Edwards, G., Howard, D., Powell, J., Keywood, M., Wang, F., 2015. Comparison of mercury concentrations measured at several sites in the Southern Hemisphere. Atmos. Chem. Phys. 15, 3125–3133.

Slemr, F., Martin, L., Labuschagne, C., Mkololo, T., Angot, H., Magand, O., Dommergue, A., Garat, P., Ramonet, M., Bieser, J., 2020. Atmospheric mercury in the Southern Hemisphere – Part 1: Trend and inter-annual variations in atmospheric mercury at Cape Point, South Africa, in 2007–2017, and on Amsterdam Island in 2012–2017. Atmos. Chem. Phys. 20, 7683–7692.

Soerensen, A.L., Sunderland, E.M., Holmes, C.D., Jacob, D.J., Yantosca, R.M., Skov, H., Christensen, J.H., Strode, S.A., Mason, R.P., 2010. An Improved Global Model for

Air-Sea Exchange of Mercury: High Concentrations over the North Atlantic. Environ. Sci. Technol. 44, 8574–8580.

Soerensen, A.L., Mason, R.P., Balcom, P.H., Sunderland, E.M., 2013. Drivers of Surface Ocean Mercury Concentrations and Air-Sea Exchange in the West Atlantic Ocean. Environ. Sci. Technol. 47, 7757–7765.

Sonke, J.E., 2011. A global model of mass independent mercury stable isotope fractionation. Geochim. Cosmochim. Acta 75, 4577–4590.

Sprovieri, F., Pirrone, N., Bencardino, M., D'Amore, F., Carbone, F., Cinnirella, S., Mannarino, V., Landis, M., Ebinghaus, R., Weigelt, A., Brunke, E.-G., Labuschagne, C., Martin, L., Munthe, J., Wängberg, I., Artaxo, P., Morais, F., de Barbosa, H.M.J., Brito, J., Cairns, W., Barbante, C., Diéguez, M. del C., Garcia, P.E., Dommergue, A., Angot, H., Magand, O., Skov, H., Horvat, M., Kotnik, J., Read, K.A., Neves, L.M., Gawlik, B.M., Sena, F., Mashyanov, N., Obolkin, V., Wip, D., Feng, X.B., Zhang, H., Fu, X., Ramachandran, R., Cossa, D., Knoery, J., Marusczak, N., Nerentorp, M., Norstrom, C., 2016. Atmospheric mercury concentrations observed at ground-based monitoring sites globally distributed in the framework of the GMOS network. Atmos. Chem. Phys. 16, 11915–11935.

Sprovieri, F., Pirrone, N., Bencardino, M., D'Amore, F., Angot, H., Barbante, C., Brunke, E.-G., Arcega-Cabrera, F., Cairns, W., Comero, S., Diéguez, M. del C., Dommergue, A., Ebinghaus, R., Feng, X.B., Fu, X., Garcia, P.E., Gawlik, B.M., Hageström, U., Hansson, K., Horvat, M., Kotnik, J., Labuschagne, C., Magand, O., Martin, L., Mashyanov, N., Mkololo, T., Munthe, J., Obolkin, V., Ramirez, Islas M., Sena, F., Somerset, V., Spandow, P., Vardè, M., Walters, C., Wängberg, I., Weigelt, A., Yang, X., Zhang, H., 2017. Five-year records of mercury wet deposition flux at GMOS sites in the Northern and Southern hemispheres. Atmos. Chem. Phys. 17, 2689–2708.

Streets, D.G., Horowitz, H.M., Jacob, D.J., Lu, Z., Levin, L., ter Schure, A.F.H., Sunderland, E.M., 2017. Total Mercury Released to the Environment by Human Activities. Environ. Sci. Technol. 51, 5969–5977.

Streets, D.G., Horowitz, H.M., Lu, Z., Levin, L., Thackray, C.P., Sunderland, E.M., 2019. Five hundred years of anthropogenic mercury: spatial and temporal release profiles. Environ. Res. Lett. 14, 084004.

Sun, R., Enrico, M., Heimbürger, L.-E., Scott, C., Sonke, J.E., 2013. A double-stage tube furnace—acid-trapping protocol for the pre-concentration of mercury from solid samples for isotopic analysis. Anal. Bioanal. Chem. 405, 6771–6781.

Szponar, N., McLagan, D.S., Kaplan, R.J., Mitchell, C.P.J., Wania, F., Steffen, A., Stupple, G.W., Monaci, F., Bergquist, B.A., 2020. Isotopic Characterization of Atmospheric Gaseous Elemental Mercury by Passive Air Sampling. Environ. Sci. Technol. 54, 10533–10543.

Vandal, G.M., Fitzgerald, W.F., Boutron, C.F., Candelone, J.-P., 1993. Variations in mercury deposition to Antarctica over the past 34,000 years. Nature 362, 621–623.

Wang, Z., Chen, J., Feng, X., Hintelmann, H., Yuan, S., Cai, H., Huang, Q., Wang, S., Wang, F., 2015. Mass-dependent and mass-independent fractionation of mercury isotopes in precipitation from Guiyang, SW China. *C.R.* Geosci. 347, 358–367.

Wang, Y., Janssen, S.E., Schaefer, J.K., Yee, N., Reinfelder, J.R., 2020. Tracing the Uptake of Hg(II) in an Iron-Reducing Bacterium Using Mercury Stable Isotopes. Environ. Sci. Technol. Lett. 7, 573–578.

Washburn, S.J., Blum, J.D., Motta, L.C., Bergquist, B.A., Weiss-Penzias, P., 2021. Isotopic Composition of Hg in Fogwaters of Coastal California. Environ. Sci. Technol. Lett. 8, 3–8.

Xu, H., Sonke, J.E., Guinot, B., Fu, X., Sun, R., Lanzanova, A., Candaudap, F., Shen, Z., Cao, J., 2017. Seasonal and Annual Variations in Atmospheric Hg and Pb Isotopes in Xi'an, China. Environ. Sci. Technol. 51, 3759–3766.

Yamakawa, A., Moriya, K., Yoshinaga, J., 2017. Determination of isotopic composition of atmospheric mercury in urban-industrial and coastal regions of Chiba, Japan, using cold vapor multicollector inductively coupled plasma mass spectrometry. Chem. Geol. 448, 84–92.

Yamakawa, A., Takami, A., Takeda, Y., Kato, S., Kajii, Y., 2019. Emerging investigator series: investigation of mercury emission sources using Hg isotopic compositions of atmospheric mercury at the Cape Hedo Atmosphere and Aerosol Monitoring Station (CHAAMS), Japan. *Environ. Sci.: Processes Impacts* 21, 809–818.

Yang, X., Jiskra, M., Sonke, J.E., 2019. Experimental rainwater divalent mercury speciation and photoreduction rates in the presence of halides and organic carbon. Sci. Total Environ. 697, 133821.

Young, D.M., Baird, A.J., Charman, D.J., Evans, C.D., Gallego-Sala, A.V., Gill, P.J., Hughes, P.D.M., Morris, P.J., Swindles, G.T., 2019. Misinterpreting carbon accumulation rates in records from near-surface peat. Sci. Rep. 9, 17939.

Yu, B., Fu, X., Yin, R., Zhang, H., Wang, X., Lin, C.-J., Wu, C., Zhang, Y., He, N., Fu, P., Wang, Z., Shang, L., Sommar, J., Sonke, J.E., Maurice, L., Guinot, B., Feng, X., 2016. Isotopic Composition of Atmospheric Mercury in China: New Evidence for Sources and Transformation Processes in Air and in Vegetation. Environ. Sci. Technol. 50, 9262–9269.

Yu, B., Yang, L., Wang, L., Liu, H., Xiao, C., Liang, Y., Liu, Q., Yin, Y., Hu, L., Shi, J., Jiang, G., 2020. New evidence for atmospheric mercury transformations in the marine boundary layer from stable mercury isotopes. Atmos. Chem. Phys. 20, 9713–9723.

Yu, B., Yang, L., Liu, H., Yang, R., Fu, J., Wang, P., Li, Y., Xiao, C., Liang, Y., Hu, L., Zhang, Q., Yin, Y., Shi, J., Jiang, G., 2021. Katabatic Wind and Sea-Ice Dynamics Drive Isotopic Variations of Total Gaseous Mercury on the Antarctic Coast. Environ. Sci. Technol. 55, 6449–6458.

Yuan, W., Sommar, J., Lin, C.-J., Wang, X., Li, K., Liu, Y., Zhang, H., Lu, Z., Wu, C., Feng, X., 2019. Stable Isotope Evidence Shows Re-emission of Elemental Mercury Vapor Occurring after Reductive Loss from Foliage. Environ. Sci. Technol. 53, 651–660.

Yuan, W., Wang, X., Lin, C.-J., Wu, C., Zhang, L., Wang, B., Sommar, J., Lu, Z., Feng, X., 2020. Stable Mercury Isotope Transition during Postdepositional Decomposition of Biomass in a Forest Ecosystem over Five Centuries. Environ. Sci. Technol. 54, 8739–8749.

Zhang, Y., Chen, J., Zheng, W., Sun, R., Yuan, S., Cai, H., Yang, D.A., Yuan, W., Meng, M., Wang, Z., Liu, Y., Liu, J., 2020. Mercury isotope compositions in large anthropogenically impacted Pearl River, South China. *Ecotoxicol. Environ. Saf.* 191, 110229.

Zheng, W., Demers, J.D., Lu, X., Bergquist, B.A., Anbar, A.D., Blum, J.D., Gu, B., 2019. Mercury Stable Isotope Fractionation during Abiotic Dark Oxidation in the Presence of Thiols and Natural Organic Matter. Environ. Sci. Technol. 53, 1853–1862.

Zheng, W., Hintelmann, H., 2010. Nuclear Field Shift Effect in Isotope Fractionation of Mercury during Abiotic Reduction in the Absence of Light. J. Phys. Chem. A 114, 4238–4245.

Zheng, W., Obrist, D., Weis, D., Bergquist, B.A., 2016. Mercury isotope compositions across North American forests: Mercury Isotopes Across U.S. Forests. *Global Biogeochem. Cycles* 30, 1475–1492.

Zhou, J., Obrist, D., Dastoor, A., Jiskra, M., Ryjkov, A., 2021a. Vegetation uptake of mercury and impacts on global cycling. Nat. Rev. Earth. Environ. 2, 269–284.

Zhou, J., Wang, Z., Zhang, X., Driscoll, C.T., 2021b. Measurement of the Vertical Distribution of Gaseous Elemental Mercury Concentration in Soil Pore Air of Subtropical and Temperate Forests. Environ. Sci. Technol. 55, 2132–2142.